ADVANCING EARTH AND SPACE SCIENCES

JGR Planets

RESEARCH ARTICLE
10.1029/2025JE009257

Key Points:

- We produced microcraters in olivine using Fe metal dust impactors electrostatically accelerated to speeds between 0.3 and 20 km s^{-1}
- We characterized the microstructures in the microcraters by scanning electron microscopy/transmission electron microscopy and correlated the observations with impact speed estimations
- Impacts at 3–4 km s^{-1} can efficiently melt olivine grains but can't act alone to form metallic Fe nanoparticles in this melt

Correspondence to:
R. Christoffersen,
roy.christoffersen-1@nasa.gov

Citation:
Christoffersen, R., Loeffler, M. J., Kanee, S., Cline, C. J., II, Keller, L. P., Erickson, T. M., et al. (2026). Experimental hypervelocity dust impacts in olivine—multiscale insights into microcrater shock and melting effects from coordinated SEM/TEM observations. *Journal of Geophysical Research: Planets*, *131*, e2025JE009257. https://doi.org/10.1029/2025JE009257

Received 25 JUL 2025
Accepted 17 FEB 2026

Author Contributions:
Conceptualization: R. Christoffersen, M. J. Loeffler, L. P. Keller
Data curation: R. Christoffersen
Formal analysis: R. Christoffersen, M. J. Loeffler, S. Kanee, C. J. Cline II, J. Fontanese
Funding acquisition: L. P. Keller, T. Munsat, M. Horányi
Investigation: R. Christoffersen, M. J. Loeffler
Methodology: R. Christoffersen, M. J. Loeffler, S. Kanee, C. J. Cline II, T. Munsat
Project administration: M. J. Loeffler
Resources: M. J. Loeffler, T. Munsat

Experimental Hypervelocity Dust Impacts in Olivine—Multiscale Insights Into Microcrater Shock and Melting Effects From Coordinated SEM/TEM Observations

R. Christoffersen[1], M. J. Loeffler[2], S. Kanee[1,3], C. J. Cline II[4], L. P. Keller[4], T. M. Erickson[1], J. Fontanese[5,6], T. Munsat[7], and M. Horányi[5,6]

[1]Amentum, NASA Johnson Space Center, Houston, TX, USA, [2]Department of Astronomy and Planetary Science, Northern Arizona University, Flagstaff, AZ, USA, [3]Now at Department of Earth & Environment, Boston University, Boston, MA, USA, [4]NASA Johnson Space Center, Houston, TX, USA, [5]Laboratory for Atmospheric and Space Physics, University of Colorado, Boulder, CO, USA, [6]NASA SSERVI's Institute for Modeling Plasma, Atmospheres and Cosmic Dust (IMPACT), University of Colorado, Boulder, CO, USA, [7]Department of Physics, University of Colorado, Boulder, CO, USA

Abstract The flux of solar system meteoroids is dominated by objects less than 1 mm in diameter whose impact effects play a major role in the space weathering of airless body surfaces. These effects remain poorly characterized with respect to their dependence on the range of impact speeds for meteoroids across the inner solar system. We investigated this dependence specifically for the mineral olivine using an electrostatic dust accelerator to bombard olivine single crystals with a stream of Fe metal dust particles traveling at measured speeds between 0.3 and 20 km s^{-1}. The impacting particles produced microcraters 0.2–5.2 μm in diameter whose content of impact melt, and brittle/ductile shock-induced deformation features, were characterized by scanning and transmission electron microscopy. While particles traveling <1 km s^{-1} were not able to form microcraters, analysis of the size versus speed relations for the faster particles allowed their impact speeds and maximum shock pressures to be statistically constrained. Microcraters 0.2–0.5 μm in diameter contain olivine-composition shock melt estimated to have formed at impact speeds as high as 15–20 km s^{-1}, and shock pressures more than 250 GPa. Transmission electron microscope studies of shock melt in larger, ∼1.5 μm diameter, microcraters found it was free of impact-generated nanophase metallic Fe ($npFe^0$). The impact speeds for these craters of 3.0–5.0 km s^{-1} suggest that in asteroid regoliths dominated by olivine, still higher impact speeds may be necessary to allow $npFe^0$ to be produced.

Plain Language Summary The population of meteoritic objects that strike the surfaces of Solar System airless bodies is dominated by particles that are millimeters to micrometers in size. Although small, the accumulating hypervelocity impact effects of these particles dramatically alter airless body surfaces in a process known as space weathering. The alteration in each impact is, however, dependent on the particle's impact speed, and the current understanding of this relationship is only qualitative. We improved this understanding of the mineral olivine by bombarding samples with Fe metal dust particles traveling at 0.3–20 km s^{-1}. The particle impacts made microcraters 0.1–5 μm in diameter, which we studied using scanning electron and transmission electron microscopy. Most, but not all, of the dust impacts were able to create microcraters that contained melted olivine, but the melting process did not generate the Fe-bearing nanoparticles that are ubiquitous in natural space weathered material. The dust impacts also produced successive zones of nanoscale fracturing and plastic deformation around each microcrater. Correlating these observations with the estimated impact speeds for specific microcraters enabled us to place new constraints on how varying micrometeorite speeds contribute to space weathering on airless body surfaces dominated by olivine.

1. Introduction

The total flux of meteoroids impacting the surfaces of solar system airless bodies is dominated by objects less than 1 mm in diameter whose accumulating impact effects play a major role in altering the top-most layers of airless body surface regoliths, as well as exposed rock surfaces (Denevi et al., 2023; Grun et al., 2011; Hapke, 2001). Although some of this alteration involves simple grain size reduction from shock-induced mechanical fracturing, many of these small-scale impacts are from micrometeoroids going fast enough (e.g., 6–20 km s^{-1} and higher) to locally melt and vaporize the target material. The melt and vapor products that accumulate from these small-scale

Software: J. Fontanese, T. Munsat
Supervision: L. P. Keller
Validation: R. Christoffersen, M. J. Loeffler, S. Kanee, T. Munsat
Writing – original draft: R. Christoffersen
Writing – review & editing: R. Christoffersen, M. J. Loeffler, S. Kanee, C. J. Cline II, L. P. Keller, T. M. Erickson, J. Fontanese, T. Munsat

impacts are not optically neutral. They contain Fe-bearing optically active nanophase particles whose progressive accumulation over time makes a major contribution to airless body surfaces becoming optically space weathered (Denevi et al., 2023; Hapke, 2001; Taylor et al., 2001). Given that these particles are dominantly metallic they are referred to here as $npFe^0$ with the understanding that a given sample can have subsets of particles with mixed oxidation state or with other elements bonded to Fe (e.g., sulfides) (Denevi et al., 2023). Despite the current broad understanding that small-scale impacts from micrometeoroids play a key role in causing space weathering, major gaps remain in connecting the effects observed in returned samples (as well as remotely) to the varying speed, size and mineralogy of solar system micrometeoroids. This includes, e.g., a lack of calibration of the threshold set of impact conditions, and target compositions, under which $npFe^0$ particles will be produced during micrometeorite impacts. Although on-going characterization of natural, impact-generated, space weathering products from both the Moon and asteroids will continue to help answer these questions, it remains true that even for a simple, single, micrometeorite impact crater on a lunar rock (e.g., Cymes et al., 2024; Noble et al., 2015, 2016; Schaal et al., 1976), the speed of the impactor that produced the crater is largely unknown.

An alternative to studying the products of natural small-scale impact products in meteorites and lunar samples is to perform hypervelocity impact and related types of experiments designed to mimic the conditions found in natural small-scale impacts (see Denevi et al., 2023). For projectile impact experiments employing chemical propulsion techniques, it has typically been possible to attain 7–8 km s^{-1} impact speeds that cover the middle-to-lower portion of the speed distribution of inner solar system meteoroids (Pokorny et al., 2019). However, the recovered experimental samples from these experiments have so far only partially resembled impact-processed natural lunar and asteroidal regoliths, with the most notable difference being a lack of $npFe^0$ particles in the experimental impact melts. It has been speculated that this may reflect impact speeds that are still too low to trigger the needed shock and thermal conditions to drive the required combination of melting, vaporization and Fe reduction in the samples in question. To bridge this perceived gap in conditions, pulsed laser experiments are now routinely used to melt and vaporize Fe-bearing target materials in such a manner as to produce abundant nanometer-sized particles of metallic Fe, that closely resemble those in natural samples (e.g., Sasaki et al., 2001). The nature of the optical-to-thermal coupling in laser irradiation has intrinsic physical differences from physical impacts, however, making it difficult to establish a quantitative link between the products of laser irradiation experiments, and effects from an individual micrometeoroid impacting at a particular speed.

Complementary to the use of chemically propelled impactors and pulsed lasers, Van de Graaf-type electrostatic accelerators have been employed since the post-Apollo era to accelerate dust-size impactors to impact speeds up to 50 km s^{-1} (Bloch et al., 1971; Fiege et al., 2019; Li et al., 2014; Mocker et al., 2011; Shu et al., 2012). This much higher range of speeds is achieved at the expense of using projectiles no larger than a micrometer. Compared to pulsed lasers, however, the effects in each small dust impact have the advantage of being a closer physical analog to the dynamics occurring in natural small-scale impacts. The physical scale of the dust impacts occurring in Van de Graaf beam lines is nevertheless very small, with the typical impact products coming in the form of microcraters, whose dimensions are rarely larger than a micrometer (e.g., Fiege et al., 2019). For this and other reasons, Van de Graff-based impact studies have tended to focus on high-sensitivity instrumentation studies of phenomena such as ionization and chemical/radiation emission as they occur at the impact site in real time (Altobelli et al., 2019; Hillier et al., 2012). Studies of impact features, such as microcraters, latent on the target material itself have been performed in a limited way by scanning electron microscopy (SEM) and other techniques, but these have mainly been limited to studies of crater physical dimensions and surface morphological features (Fiege et al., 2019; Li et al., 2014).

In the current study, we have been motivated to more fully explore the connection between the impact speeds attained in electrostatic dust accelerator experiments and the impact products contained in the resulting microcraters by combining transmission electron microscope (TEM) techniques with the more commonly employed approaches based on SEM. Olivine was selected for the study because it is a major constituent in asteroidal surface regoliths, particularly those on S-type bodies such as the asteroid Itokawa (Nakamura et al., 2011). Calibrating olivine's response to small-scale impacts of increasing speed, including the critical speed at which shock melting occurs and $npFe^0$ may be generated, is therefore critical for understanding the role of impacts in the space weathering of these and other asteroids. Consistent generation of appreciable shock melt in olivine targets remains at the margin of what is possible at the 6–7 km s^{-1} maximum speed of chemically propelled experimental projectiles (Bauer, 1979). We were therefore interested to investigate the higher speed capabilities of an electrostatic accelerator for obtaining improved constraints on the threshold speeds for both shock melting and shock-related deformation of olivine under micrometeoroid impacts.

2. Experimental Methods

2.1. Experimental Dust Impact Facilities, Samples and Conditions

We performed dust impact experiments using the Dust Accelerator Laboratory (DAL) at the Institute for Modeling Plasma, Atmospheres and Cosmic Dust (IMPACT) at the University of Colorado (Shu et al., 2012). The DAL is 3 MV Pelletron generator in which a dust particle source is mounted onto the high voltage terminal of the Pelletron and individual charged dust particles receive a known charge and are accelerated into the beam line by the electrostatic field (Shu et al., 2012). A set of pick-up tube speed sensors and gating circuits record the speed of each particle and admit it to the target according to its measured speed compared to a preselected range of values. The mass of the particle that strikes the target can be calculated by its measured speed, electrostatic charge and beam line accelerating voltage. Sample impact occurs in a target chamber maintained at a vacuum to 10^{-7} torr, with the target aligned using a beam axis laser positioned an additional 8.6 m along the beam line from the target. The dust beam has a Gaussian profile with a ∼6 mm diameter, set by the 1 mm aperture at the source and subsequent expansion, and constrained by the 9 mm diameter apertures of the velocity pick-up tubes.

We used Fe metal dust impactors for the current experiments that are pulled into the accelerator tube from a powdered reservoir by electrostatic levitation (Shu et al., 2012). Previous SEM studies of these types of metallic nanoparticles, whether Fe, Cu or other metals, show that individual particles can have complex cluster-like shapes (e.g., Fiege et al., 2019). The accelerator gating circuitry was set to admit all particles with velocities between 0.35 and 30 km s^{-1}, a broad range corresponding to operation of the beam line with minimal velocity gating. A total of two dust impact experiments were performed under the same conditions as described above, but for different total particle counts of 10,000 (10k experiment) and 40,000 (40k experiment).

The target material in each experiment was a cm-sized, gem-quality single crystal of San Carlos olivine. Based on the methods described below, quantified SEM and TEM energy-dispersive X-ray spectroscopy analyses showed that the crystals had the same average compositions within error of $(Mg_{0.87}Fe_{0.13})SiO_4$, with a high degree of compositional homogeneity as typically reported for this material (Fournelle, 2011). Prior to loading into the sample chamber, we trimmed each crystal with a wafering saw to create a flat, roughly square target surface with approximate dimensions of 5 × 8 mm, and a thickness in the beam direction of 2–3 mm. We then embedded each crystal in 1 cm-diameter cylindrical epoxy blocks and ground to expose a flat clean crystal surface. Final polishing followed standard electron beam preparation protocols using 30 μm alumina-embedded polymer film media for the initial surface finish, followed by sequential polishing with 6 to 1 μm diamond in a water-based suspension. We cleaned the final polished surface in high-purity ethanol and examined it for surface defects and cleanliness using a reflected light optical microscope. Based on electron diffraction patterns of focused ion beam (FIB) sections extracted normal to the sample surface, the 40K experiment sample surface was determined to be approximately parallel to the (−1–52) olivine crystallographic plane. We did not determine the crystallographic orientation of the sample surface for the 10K experiment.

2.2. Sample Characterization

Dust impacts on the samples produced microcraters that were identified and characterized using a 200 kV JEOL 7600 field-emission analytical scanning electron microscope at NASA Johnson Space Center (JSC). This instrument is equipped with a Thermo® energy-dispersive (EDS) silicon drift detector (SDD) X-ray spectrometer system, and associated Thermo® NSS software for standardless EDS analysis quantification and automated image acquisition. Conventional TEM bright-field (BF)/dark-field (DF) imaging was performed at a beam current of 1 nA. STEM imaging and scanned probe analyses were performed at 2.5 nA.

Initial SEM imaging of the samples established several morphological criteria to distinguish impact-generated microcraters from other surface pits and depressions not generated by impact. The most reliable of these was the presence of impact-melted residue from the Fe metal dust impactor in and around a given surface depression. The residue showed distinctive bright contrast in the back-scattered electron (BSE) images, taking the form of spherules and splash-shaped patches adhering to the microcrater walls and floor. It was consistently well

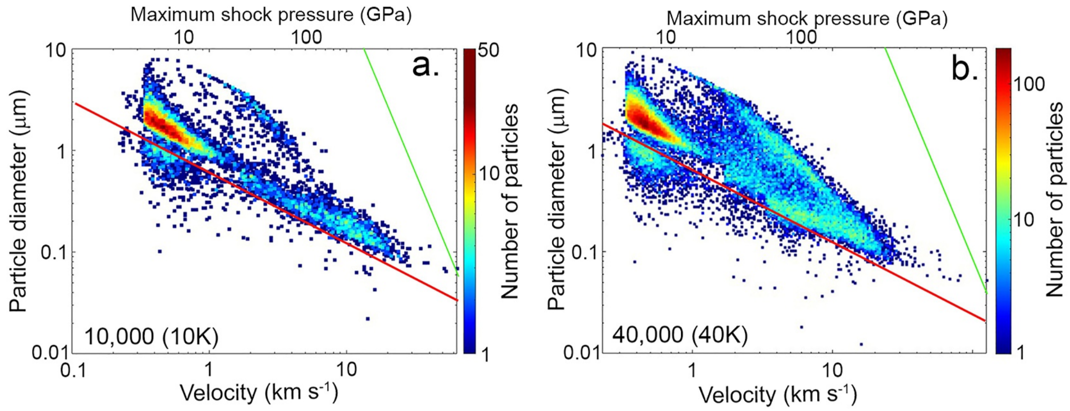

Figure 1. Number of electrostatically accelerated Fe metal dust particles as a function of their equivalent-sphere diameter and speed for dust impact experiments into San Carlos olivine single crystals. Data correspond to sensor-counted particles that were gated into the accelerator sample chamber based on measured velocities between 0.3–30 km s^{-1}. The upper green line defines the fractional field emission limit controlling the maximum voltage a particle can maintain as a function of its size. The lower red line defines the lower limit of charge that can be detected for gating into the sample chamber. Upper shock pressure scale equals the maximum shock pressures corresponding to lower scale impact velocities based on shock impedance calculations summarized in Appendix A. (a) Data for 10K experiment performed using a total of 10,000 detected and gated particles. (b) Data for 40K experiment performed using 40,000 detected and gated particles.

correlated with other morphological and microstructural features in microcraters that were also indicative of formation by impact, as described below.

After identifying the characteristics of impact-generated microcraters on the samples, an automated imaging survey was conducted to perform a total microcrater count across the entire surface of the samples. This utilized the Thermo® automated grid-registered secondary electron imaging software to acquire 1,500 to 1,800 overlapping image frames at a frame magnification of 500X. The frames were then manually inspected offline to identify and count microcraters. Based on the digital image resolution of the frames of 0.235 µm $pixel^{-1}$ the count was estimated to be limited to only identifying microcraters greater than 0.75 µm in diameter. Subsequent SEM work, described below revealed that the samples contained a considerable (but not counted) number of smaller microcraters below this size, such that the automated count results should be taken to represent minimum values.

During the process of examining each 500X image frame to count microcraters, a sub-set of identified microcraters was tagged for follow-up SEM imaging under optimum magnification and image resolution conditions. This work was performed primarily on the 40K sample because of its higher population of identifiable microcraters. A final round of operator-directed high-magnification imaging was then performed to search for and characterize smaller microcraters below the 0.75 µm diameter size visible in the automated images. The objective of this work was not to obtain a fully accurate count of these smaller craters, but to assess their overall characteristics given that they were likely made by the smaller, higher-speed, impactors in the impactor population (see Figure 1 and discussion below).

For the sub-set of microcraters studied in detail by SEM imaging, we measured the size and shape of microcraters by tracing the 2-dimensional outline of crater rims and parameterizing the resulting shape using the region-of-interest (ROI) measurement tool in the image analysis software ImageJ®. For the microcrater sizes reported below, we used the diameter of a circle equivalent in area to the traced crater rim outline. For describing microcrater shape, we report several shape parameters computed by the ImageJ software that we judged potentially useful for evaluating shape variations as a function of microcrater diameter.

During the SEM characterization of the samples, we selected a subset of three microcraters from the 40K sample to be prepared by FIB cross sectioning for TEM imaging and microanalysis. We performed FIB sectioning at NASA JSC utilizing an FEI Quanta 3D dual focused ion/electron beam instrument with a Ga ion milling source. For TEM imaging and microanalysis, we used a 200 kV JEOL2500SE field-emission scanning transmission electron microscope (FE-STEM) at NASA JSC. This instrument is capable of conventional and high-resolution TEM digital imaging, as well as both BF and high angular annular dark field Z-contrast imaging in STEM mode.

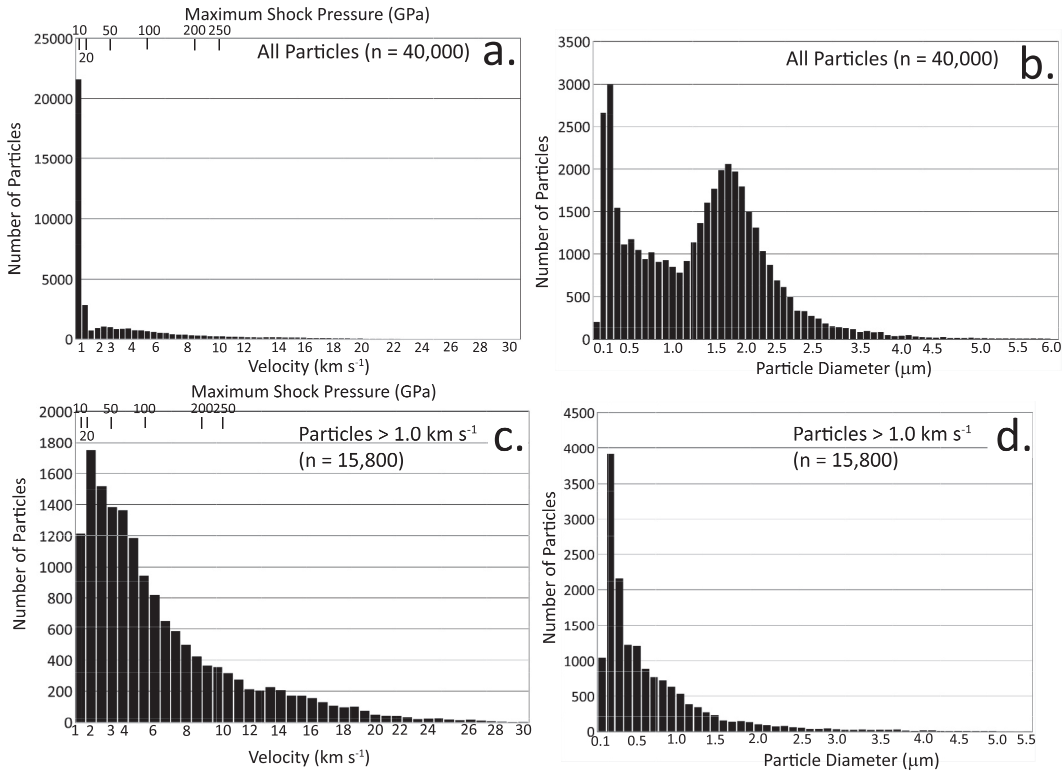

Figure 2. Speed and size distribution histograms for 40K Fe metal dust impact experiment on San Carlos olivine single crystals. Binning intervals determined by Scott's rule (Scott, 1979). (a) Speed and (b) size distribution histograms for the entire population of 40,000 sensor-counted particles that were gated into the accelerator sample chamber based on measured velocities between 0.3–30 km s^{-1}. (c) Speed and (d) size distribution histograms for the fraction of 15,800/40,000 particles whose speeds exceed a hypothesized minimum 1.0 km s^{-1} threshold for forming microcraters.

Capabilities for chemical microanalyses are provided by a JEOL 60 mm^2 silicon drift energy-dispersive X-ray detector (SDD) supported by a Thermo® NSS analyzer optimized for nm-scale quantitative compositional spectrum image chemical mapping. The Thermo® quantification routine for chemical maps as well as spot analyses utilized empirically determined k-factors based on the Cliff-Lorimer method (Cliff & Lorimer, 1975). We typically acquired chemical maps using a 2 or 4 nm probe with multiple frame integration and a short probe dwell time to limit beam damage during map collection.

2.3. Shock Pressure Calculations From Impedance Matching

Shock pressures generated in the single-crystal olivine target material as a function of the speed of the impacting Fe metal dust particle were modeled using shock impedance matching techniques. Model input parameters, which included Hugoniot data from Marsh (1980) for Fe metal and Ahrens and Johnson (1994; and reference therein) for olivine, are listed in Table A1. Results are tabulated and graphed in Table A2 and Figure A1 respectively. Shock pressures corresponding to impact speeds are also shown on secondary shock pressure scales in Figures 1, 2, and 11. Given the monophase nature of the projectiles, the recorded impact speed was used to convert into the maximum pressure generated in each impact. It is important to note that this maximum pressure would only be expected at the point of contact, because the shock state experienced by the sample decays as a function of distance from the point of impact.

3. Results

3.1. Dust Particle Size-Speed Distribution

The distribution of the measured speeds and equivalent-sphere diameters of the Fe-metal dust particles in the 10 and 40K experiments are shown in the heat-plot diagrams in Figure 1 and in the separate speed and size histograms in Figures 2a and 2b. The speed plots include secondary shock pressure scales derived from the shock pressure versus impact speed relations in Appendix A. Regarding Figure 2 histograms, it is important to note that the separate speed and size distributions describe an overall population in which these two variables are only broadly, and complexly, correlated (see below). The histograms must therefore be carefully interpreted regarding how a given speed interval on one corresponds to a size interval on the other (and vice versa).

Figure 1 heat plot distribution has a characteristic shape that reflects limitations or boundaries imposed by the dust accelerator technological design (Shu et al., 2012). The lower boundary (red line, Figure 1) is defined by the lowest detectable particle charge that the system can measure and gate into the sample chamber. The upper boundary of the distribution reflects limitations imposed by the so-called field emission limit (green line, Figure 1), which limits the maximum charge that the system can impose on particles as an inverse function of their mass. This limit decreases the average size of particles that can be accelerated to higher velocities and restricts their range of sizes at these higher velocities. Due to the different slopes of the upper (green) and lower (red) boundaries there is a broad negative correlation of particle speed with size, such that faster particles tend to have smaller sizes, and slower particles are relatively larger. The specific sub-population of slower and larger particles that have speeds <1 km s^{-1} and sizes >1 μm make up ∼70% of the total particle populations. These particles occupy the high concentration regions in the upper left quadrants of Figure 1, as well as the largest speed and size bins in Figure 2 histograms. The calculated maximum shock pressures generated by impacts from these particles are all <15 GPa (Figure 2a, Appendix A).

For the population of particles with speeds >1 km s^{-1} a local minimum occurs in the mid-speed (1–3 km s^{-1}) and mid-size (0.3–1 μm) regions of the distribution (Figures 1 and 2), with a secondary peak occurring as speeds increase into the 3–6 km s^{-1} range. The remaining 20% of particle speeds and sizes above this secondary peak occupy a gradually decreasing tail of highest speed (>3 km s^{-1}) and smallest size (<0.3 μm) particles. Maximum shock pressures calculated for these higher speed particles range from ∼50 GPa at 3 km s^{-1} up to 250 GPa at 10 km s^{-1}. For the approximately 10% of particles whose speeds extend into the 10–25 km s^{-1} range, shock pressures could theoretically extend as high as 500 GPa, assuming reasonable continuity of Figure A1 functional relations into this speed regime.

3.2. SEM Microcrater Counting and Microstructural Characterization

Microcraters in the 10 and 40K samples appear as pit-like surface depressions that generally have ovoid outlines but can also be irregular and jagged in the case of some of the larger microcraters (Figures 3, 4, and 5). We did not identify any confirmed microcraters smaller than 0.2 μm in diameter or larger than 5.2 μm in diameter in the 40K sample (Table 1). Figure 6 shows the number and spatial distribution of larger (>0.75 μm) microcraters in the 10 and 40K samples as obtained from the auto-acquired SEM secondary-electron image frames. The distribution of microcraters across the samples is not homogeneous with significant areas showing no microcraters >0.75 μm in diameter (Figure 6). We did not systematically search these nominally blank regions in follow-on SEM work to see if they might contain microcraters too small to be identified in the auto-acquired images, but instead gave preference to studying areas already shown to contain microcraters. For the 40K sample, there is a near-circular curvature to the boundary between the crater-containing area concentrated in the lower right of the sample and the blank area on the upper left (Figure 6). The curvature suggests that the accelerator dust beam, whose shape is controlled by a circular aperture in front of the sample chamber, may have been off-center relative to the center of the sample. If allowance is made for this possibility, and a geometrical correction is applied based on the average microcrater density in the lower right portion of the sample, the total number of microcraters >0.75 μm in diameter on a fully irradiated the sample would have been expected to be approximately 4,800 instead of 1,864 (Figure 6).

We performed detailed SEM imaging studies on a total of 31 confirmed microcraters in the 40K sample and summarize their size, shape and basic descriptive information in Table 1. SEM images for a representative subset of these microcraters are shown in Figures 3, 4, and 5. Microcrater shapes and microstructures varied with respect to: (a) the shape of crater rim outlines (e.g., circular-to-ovoid-to-irregular), (b) the degree to which crater interiors and rims exhibit brittle deformation features (e.g., microfractures in and around the crater cavity), and (c) the presence or absence of smooth material partially lining microcrater cavities and/or covering their rims. As described in detail below, we used correlated SEM and TEM studies to confirm that this smooth material consisted of shock melt generated from the olivine target material. Spherules and splat-like patches of shock melt generated from the Fe metal dust impactors are also present within and around the microcrater cavities (Figures 3,

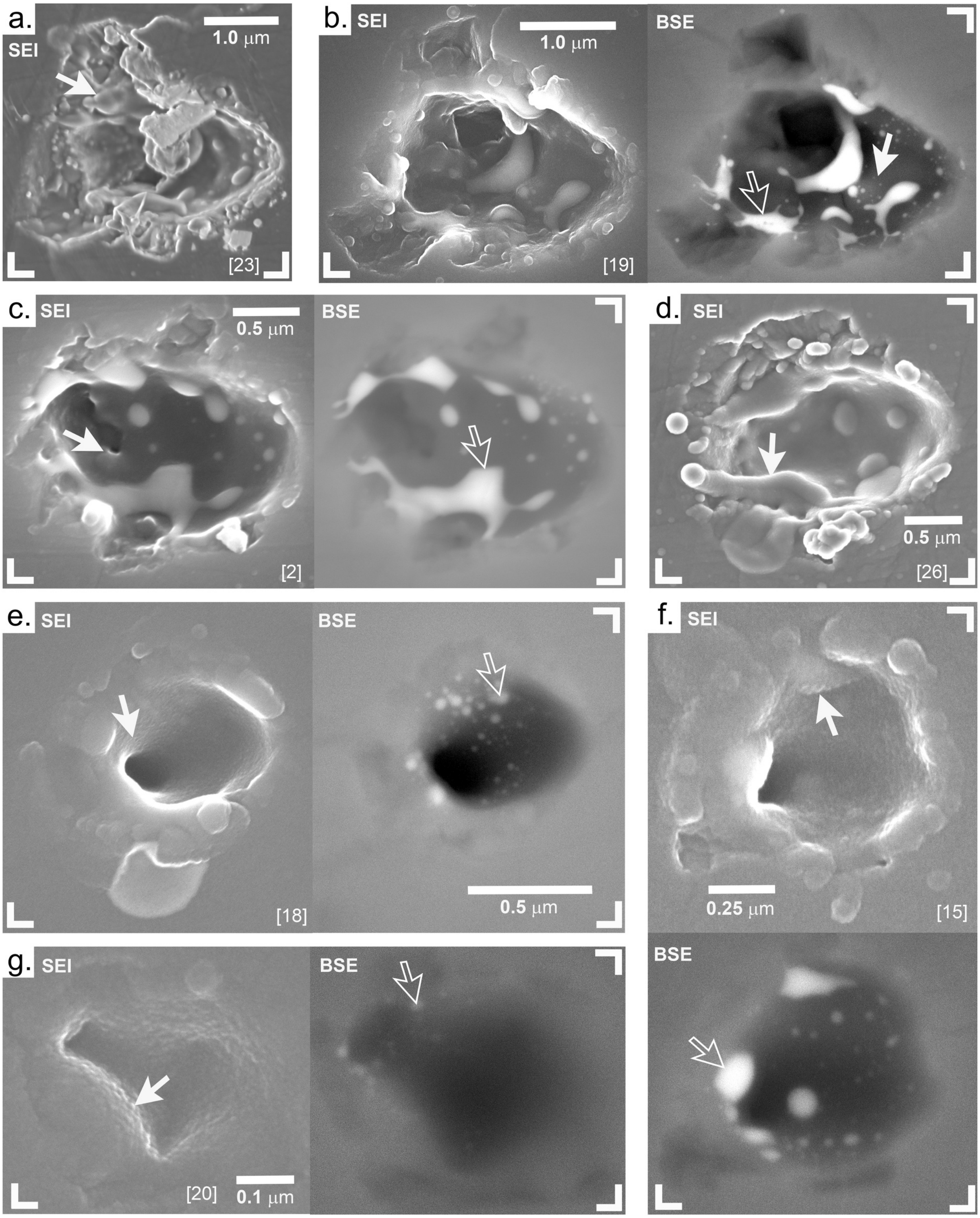

Figure 3. Scanning electron microscopy images of dust-impact microcraters in an olivine single crystal from 40K experiment. Images (a) and (d) are single secondary electron (SEI) images and (b, c, e–g) are paired SEI and back-scattered electron images as indicated. Numbers in square brackets are the corresponding microcrater numbers (Table 1). Microcrater diameters decrease progressively from (a) to (g) with (a) having a diameter (2.9 μm) that is approximately a factor of 10 larger than the 0.2 μm diameter microcrater in (g).

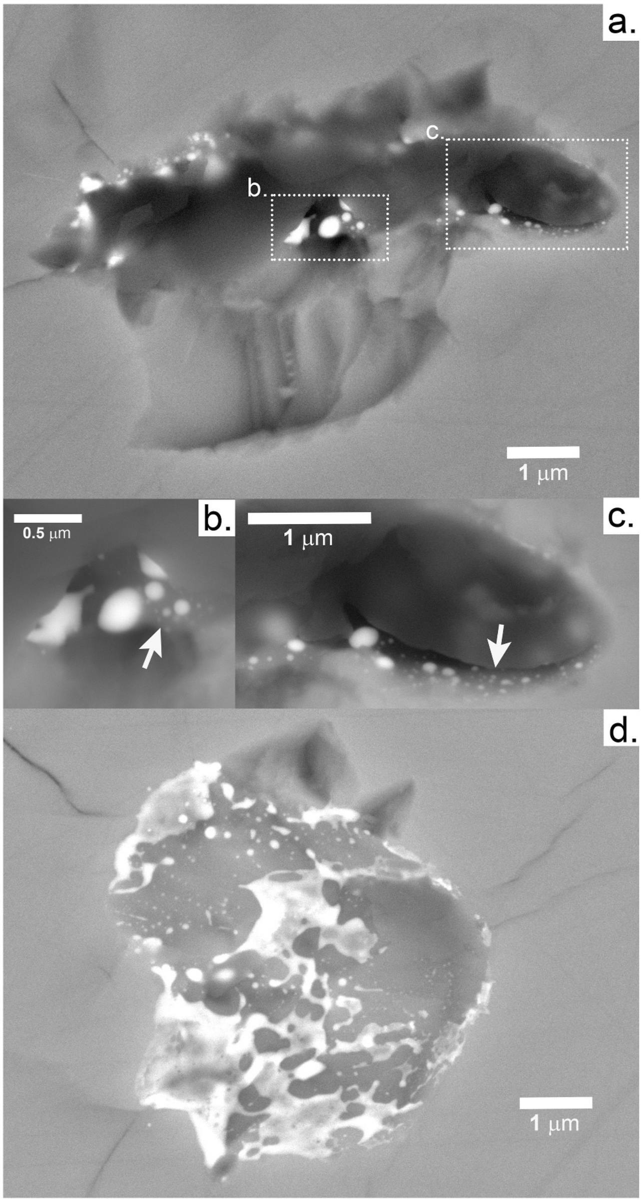

Figure 4. Scanning electron microscopy backscattered-electron images of microcraters #4 (a, b, and c), and #8 (d) in the 40K sample (see Table 1). In (a)–(d) the bright contrast spherules and splash-like patches are shock-melted remnants of the Fe metal dust impactor. Arrows in (b) and (c) show examples where Fe spherules are embedded in lower contrast smooth material that based on transmission electron microscope observations of similar material in other microcraters is interpreted to be impact melt derived from the olivine target material (see text).

4, and 5). These are distinguishable from shock melt generated from the olivine target material based on their high Z-contrast in BSE images.

Microcrater shapes are variably non-circular as indicated by the circularity parameters in Table 1. Several of the largest craters (e.g., 2–5 μm in diameter) displayed highly irregular or jagged outlines due to high degrees of spallation micro-fracturing (e.g., Figure 4). Microcraters <2 μm in diameter give the impression of having more smoothly curving or ovoid outlines, but this observation was not strongly reflected quantitatively in size-dependent trends in the applied shape parameters (Table 1).

All microcraters exhibited various types of brittle deformation features in the SEM images. These included fractures radiating away from the microcrater rims into the surrounding host olivine (e.g., Figures 4 and 5a) and "scalloping" of microcrater rims, walls and floors associated with spallation micro-fracturing (e.g., Figures 3, 4, and 5). Fresh fracture surfaces associated with spallation microcracking were typically visible in SEM images of microcraters walls and floors (e.g., Figures 4 and 5a), but many microcraters also had a portion of their floors and walls covered by smooth material that obscured underlying surfaces (Figures 3a–3c, 4a–4c, 5b, and 5c). As previously noted, some of this smooth material showed high Z-contrast in BSE images, confirming it to be shock-melted remnants from the Fe metal dust impactor (e.g., Figure 3). The remaining smooth material showed BSE contrast like that of the surrounding host olivine (Figures 3, 4, 5b, and 5c). It tended to smoothly coat portions of microcrater floors, walls and rims in a manner very different from the droplets and splash-like areas of the melted impactor (Figures 3b–3d, 3f, 4c, 5b, and 5c). Examples are also noted where metallic spherules and droplets derived from the impact material are embedded within regions of smooth material in a manner consistent with both materials being molten when they intermix (Figures 3b, 3c, 3f, 4b, and 4c). The proportion of smooth material relative to microcrater diameter tended to be smaller in larger microcraters, whereas in many of the smaller (<2 μm diameter) microcraters, the smooth material filled significant portions of the microcrater cavity (Figures 3d–3g). In smaller microcraters where the relative volume of smooth material was higher, it showed evidence of flowing out of the microcrater cavity, an aspect which along with its other features strongly suggested it was impact melt derived from the olivine target material (Figures 3d–3f). This interpretation was ultimately confirmed by subsequent TEM studies (see below). Overall, we found 21 of the 31 microcraters (68%) contained regions of likely impact melt derived from the olivine target (Table 1).

3.3. Microcrater TEM Characterization

In Figure 5, we show SEM secondary-electron images of the three dust-impact microcraters that were FIB-sectioned for FE-STEM characterization. Microcrater #1 was the third largest (3.3 μm) among the 31 microcraters studied in detail by SEM imaging (Table 1; Figure 5a). Its ovoid-to-elongate shape corresponds to an average degree of circularity relative to the other microcraters listed in Table 1. In SEM images, it shows several types of brittle deformation features including fractures extending radially into the host olivine, and spallation fracture surfaces along its rim and walls (Figure 5a). No smooth material covering any portions of its walls, rim, and floor could be seen in the SEM images (Figure 5a).

Microcraters #29 and #30, respectively 1.7 and 1.6 μm in diameter (Table 1; Figures 5b and 5c), occurred adjacent to one another with a separation of less than 15 μm that enabled them to be prepared in a single FIB section (Figures 5b and 5c). They have similar morphologies and SEM-scale microstructures (Figures 5b and 5c). Their

10.1029/2025JE009257

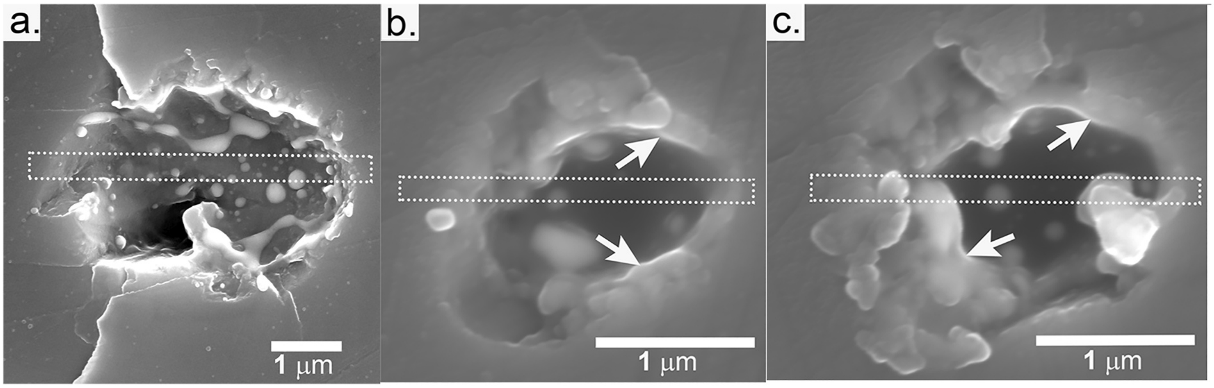

Figure 5. Scanning electron microscopy secondary electron images of microcraters #1 (a), #29 (b), and #30 (c) in the 40K sample that were prepared by focused ion beam (FIB) sectioning for transmission electron microscope (TEM) characterization (Table 1). Rectangles show the position and orientation of the FIB sections. Arrows in (b) and (c) point to smooth material lining the crater cavities that TEM imaging confirmed to be impact melt derived from the olivine target material.

rims show fracture-induced scalloping like crater #1, but portions of their rims and walls were also covered in smooth material that TEM observations confirmed to be shock melted olivine.

TEM images showing the complete FIB cross-sections of microcraters #1, #29 and #30 are shown in Figure 7. Based on TEM electron diffraction patterns, the FIB section containing microcrater #1 was determined to be approximately parallel to the (917) crystallographic plane. The single FIB section containing microcraters #29 and #30 is oriented approximately parallel to (513). In cross-section, the crater cavities for craters #29 and #30 are both bowl shaped, with respective depth-to-diameter ratios of (0.65/1.7 = 0.4) and (0.85/1.6 = 0.5) (Figures 7b and 7c). Microcrater #1 has a comparatively shallower cavity outline, with a significantly smaller depth-to-diameter ratio of (0.70/3.3 = 0.2) (Figure 7a). These relations agree with tilted-stage SEM images obtained during FIB sectioning, which showed a relatively flat bottom for microcrater #1 and bowl-shaped interiors for microcraters #29 and #30. A silicate glass layer 0.1–0.2 μm wide lines the cavity walls and floor of microcraters #29 and #30 but was not observed in microcrater #1. Quantified EDS analyses indicated that the composition of the glass layer matches the composition of the host olivine within analytical error. Both analytical and imaging observations support the interpretation that the glass is a cavity-lining layer of shock melt formed during the dust particle impact event. This finding further supports the interpretation that the patches of smooth material seen in the SEM images of microcraters #29 and #30, as well as other microcraters, is shock-generated melt. HAADF STEM imaging did not reveal any nm-sized Fe grains, metallic or otherwise, that were uniformly distributed in the middle to bottom portions of the glass layer as is typically observed for $npFe^0$ particles generated in natural microcraters or laser-irradiated samples (Fazio et al., 2018; Noble et al., 2015). However, metallic Fe in a different microstructural form is found in the FIB sections of all three microcraters as spherules or mound-shaped grains 0.1–0.5 μm in size (Figures 7–10). As identified through electron diffraction and EDS analyses, these Fe metal grains are restricted to the outer surfaces of the microcrater cavity walls and floor (Figures 7–10). Based on their resemblance to similar rounded, high-contrast grains observed in SEM BSE images, we interpret these grains to also be shock-melted remnants of the metallic Fe dust particle impactors.

The un-melted olivine around all three microcraters is highly shock deformed. Two types of deformation microstructures are observed: (a) a polycrystalline region resulting from high-density nanoscale fracturing, here referred to as the nano-fractured zone (Figures 8d, 9a, 9e, and 10b), and (b) a dislocation-dominated zone in which dislocations are arranged in complex arrays and networks of varying dislocation density (Figures 7–10). The nano-fractured zone occupies a central core region 0.5–0.7 μm deep and 1.0–1.2 μm wide located below the microcraters floors (Figures 7, 8d, 9a, 9e, and 10b). Within the zone, fractures tend to be locally aligned in a sub-parallel manner with spacings of 30–50 nm (Figures 8d, 9c, 10b). The resulting polycrystalline microstructure is composed of narrow elongate grains, which, although unfractured, nevertheless show a high degree of diffraction strain contrast. Selected-area electron diffraction patterns of this polycrystalline material show close to single-crystal zone axis patterns with only a few degrees of rotational asterism (Figure 8d). This indicates that these regions, although rendered polycrystalline by intense nano-scale fracturing, retain a strong crystallographic preferred orientation from the parent crystal. In microcrater #29, a particularly well-developed network-like

Table 1
Size and Shape Parameters for Microcraters in 40K Sample Determined by SEM Imaging

Crater #	Diameter[a] (μm)	Max. Feret dia.[b] (μm)	Min. Feret dia.[b] (μm)	Circ.[c]	Solidity[d]	Smooth material?	Olivine impact melt?	Notes
8	5.2	6.1	5.0	0.76	0.94	N	No	In Figure 4d
4	5.1	7.9	4.1	0.53	0.84	Y	Likely	In Figures 4a–4c
1	3.3	4.4	2.5	0.75	0.96	N	No, confirmed by TEM	In Figure 5a
23	2.9	3.9	2.9	0.66	0.90	Y	Likely	In Figure 3a
14	2.8	4.1	2.0	0.74	0.99	Y	Likely	
12	2.5	3.1	2.3	0.66	0.92	N	No	
19	2.3	3.2	2.5	0.58	0.82	Y	Likely	In Figure 3b
11	2.3	2.7	1.9	0.89	0.99	U	Undetermined	Poor image resolution
7	2.2	2.7	1.9	0.83	0.98	Y	Likely	
6	1.9	2.6	1.5	0.79	0.97	N	No	
2	1.8	2.1	1.6	0.86	0.98	Y	Likely	In Figure 3c
29	1.7	2.0	1.6	0.83	0.96	Y	Yes, confirmed by TEM	In Figure 5b
30	1.6	2.0	1.4	0.89	0.99	Y	Yes, confirmed by TEM	In Figure 5c
26	1.5	2.0	1.2	0.83	0.99	Y	Likely	In Figure 3d
25	1.2	1.6	0.9	0.70	0.96	U	Undetermined	Poor image resolution
13	1.0	1.3	0.9	0.79	0.99	Y	Likely	
27	1.0	1.3	0.8	0.81	0.98	N	No	
5	0.9	1.2	0.7	0.74	0.96	N	No	
9	0.8	1.1	0.6	0.80	0.98	U	Undetermined	Poor image resolution
22	0.8	0.9	0.7	0.84	0.97	Y	Likely	
18	0.6	0.7	0.5	0.85	0.99	Y	Likely	In Figure 3e
16	0.6	0.7	0.6	0.89	0.98	Y	Likely	
3	0.6	0.6	0.5	0.86	0.99	Y	Likely	
10	0.6	0.7	0.4	0.87	0.99	U	Undetermined	Poor image resolution
17	0.6	0.7	0.5	0.77	0.96	Y	Likely	
15	0.5	0.5	0.4	0.73	0.97	Y	Likely	In Figure 3f
24	0.4	0.5	0.4	0.91	0.99	Y	Likely	
31	0.4	0.5	0.4	0.93	0.00	Y	Likely	
28	0.4	0.4	0.4	0.92	0.99	Y	Likely	
21	0.2	0.4	0.2	0.71	0.98	Y	Likely	
20	0.2	0.3	0.2	0.76	0.93	Y	Likely	In Figure 3g

Note. Microcraters containing smooth material corresponding to impact melt generated from the olivine target material are indicated (see text). Smooth material = Y (68%), N (19%), U (13%). [a]Diameter of circle with area equal to that of the traced microcrater rim outline. [b]Feret diameter (max/min)—longest/shortest distance between any two points along the traced microcrater rim outline. [c]Circularity = 4π x [area of microcrater outline]/[microcrater perimeter]^2; measures shape elongation relative to circle = 1.0. [d]Solidity = [area of microcrater outline]/[convex area of outline]; measure the degree of re-in the crater outline.

arrangement of the microfractures occurs (Figure 9e). Within this network, several of the intersecting regions between fractures contained olivine-composition amorphous material that likely represents shock melt which formed locally within the fracture network due to frictional melting or infiltrated into the network from the pool of shock melt lining the microcrater cavity. The nano-fractured zone transitions to the dislocation-dominated zone across a narrow boundary zone 100–200 nm wide (Figures 7–10). In most examples, the boundary is a region of very dense strain contrast in which individual dislocations are not resolvable until the boundary is crossed into the dislocation-dominated zone where dislocations can be imaged at densities of $\sim 10^{14}$–10^{13} m^{-2} (e.g., Figures 8a, 8c, and 10a). Less commonly, the boundary is sharply defined by fault-like linear defects that occur on the left-side regions of microcraters #29 and #30 (Figures 7b, 7c, and 9a). Within the dislocation-dominated zone itself,

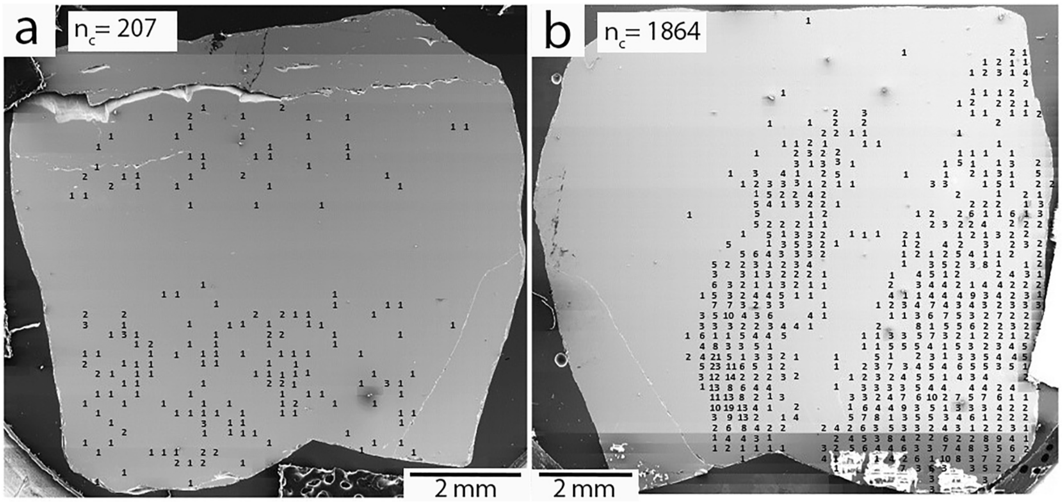

Figure 6. Scanning electron microscopy secondary electron image mosaics of the (a) 10K (a) and (b) 40K single crystal olivine samples showing the distribution of dust-impact microcraters greater than 0.75 μm in diameter. Mosaics were constructed from 1,500 (10K) and 1,800 (40K) auto-acquired grid-registered secondary electron image frames taken at 500X magnification. Overlayed numbers are the number of microcraters manually counted in each 500X frame. Total counts (n_c) for microcraters >0.75 μm in diameter are listed in the upper left.

dislocations typically form arrays of parallel dislocation line segments, some of which terminate in hook-shaped partial loops (Figures 7, 8c, 9a, 10a, and 10c). The Burgers vectors **b** for these dislocations were determined based on $\boldsymbol{g} \cdot \boldsymbol{b}$ contrast extinction experiments performed under conventional two-beam BF conditions (Hirsch et al., 1977; Williams & Carter, 1996). Figures 8a and 8c show the contrast conditions under which a high density of dislocations around microcrater # 1 is visible under symmetrical [100] zone axis diffraction conditions. Of the known [001] and [100] Burger vectors for olivine only $\boldsymbol{b}$ = [001] dislocations are visible under these conditions (Carter & Ave'Lallement, 1970; Barber et al., 2010). In Figure 8b, a two-beam experiment for $\boldsymbol{g}$ = 020 shows nearly complete extinction for the entire set of $\boldsymbol{b}$ = [001] dislocations visible in Figures 8a and 8c, consistent with the [001] Burger's vector identification from Figures 8a and 8c. To rule out the presence of $\boldsymbol{b}$ = [100] dislocations in addition to the $\boldsymbol{b}$ = [001] set, we performed a set of two-beam contrast experiments using reflections in the class hk0, for which [001] dislocations are extinct, but [100] dislocations are visible. In Figure 9b, a two-beam image of the left side of microcrater #29, using only the 170 reflection, produces nearly complete extinction of all the dislocations visible in the corresponding [100] symmetrical zone axis image (Figure 9a). These results rule out the presence of any $\boldsymbol{b}$ = [100] dislocations in the imaged region. We obtained similar results from contrast experiments performed on microcraters #1 and #30.

For $\boldsymbol{b}$ = [001] dislocations in olivine, the corresponding slip planes have been previously shown to be dominantly restricted to the {110} prism set (Carter & Ave'Lallement, 1970; Barber et al., 2010). Using methods discussed by Head et al. (1973), we found the {110} set of slip planes to be the ones most consistent with the direction of dislocation line segments in symmetric zone axis images (e.g., Figure 8c). The tendency for dislocation line segments to be generally straight and aligned with the projection of the [001] Burger's direction in most TEM images suggests that these segments dominantly have screw character. Where these screw segments terminate in hook-shaped partial loops, the corresponding shorter edge segments are visible (Figures 8c and 10a). The microstructure is consistent with dislocation loops being highly elongated in the Burger's vector direction, likely due to relative differences in screw versus edge segment mobility, as discussed below.

4. Discussion

4.1. Influence of Low-Speed Particles on Microcrater Formation

For both the 10 and 40K samples, we found an order of magnitude discrepancy between the number of Fe metal dust particles counted entering the sample chamber and the number of observed microcraters on the samples. For the 40K sample, for which we have the more extensive SEM observations, the ratio of observed microcraters to

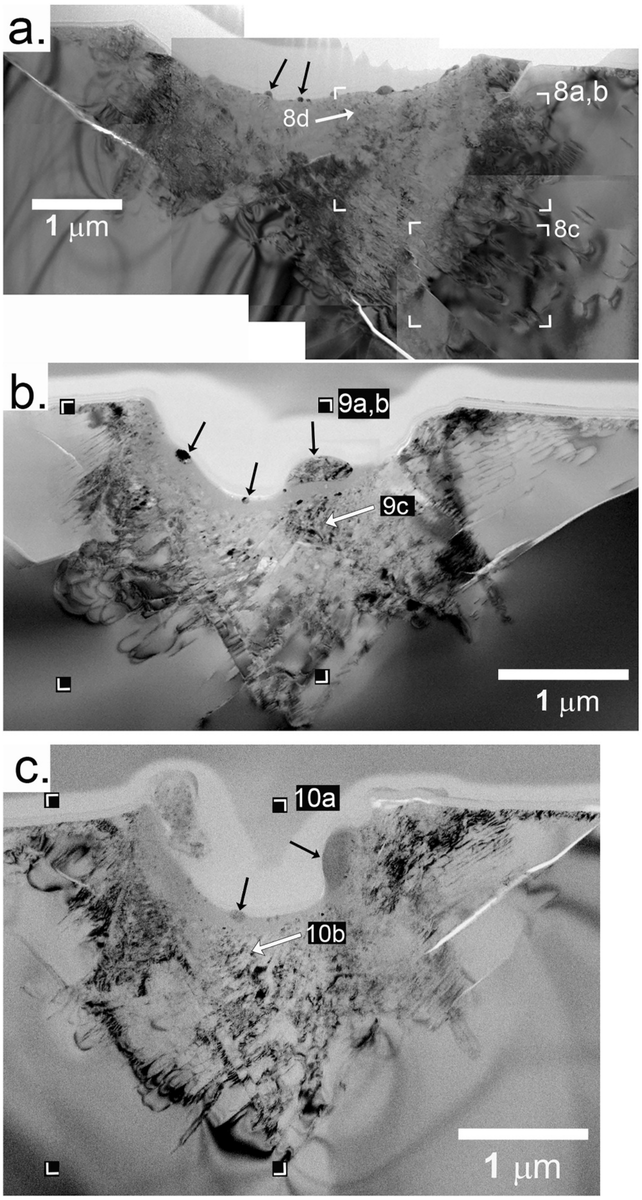

Figure 7. Transmission electron microscope (TEM) images of the focused ion beam sections prepared from microcraters #1 (a), #29 (b) and #30 (c). (a) Montage of conventional TEM bright-field diffraction contrast images. (b, c) Inverted contrast dark-field diffraction contrast STEM images. In all three microcraters, the principal impact-induced microstructures in the olivine include dense nano-scale fractures immediately below the microcrater floors and dislocations surrounding the nano-fractured region. Microcraters #29 and #30 also exhibit glassy impact melt linings along their crater cavity walls. Metallic Fe spherules derived from shock melting of the Fe metal dust impactor are shown by the black arrows. Corner markers and white arrows reference key microstructural regions shown in greater detail in Figures 8–10.

counted (i.e., 40K) particles is ∼0.05 based on the un-corrected microcrater count of 1,864 for microcraters >0.75 μm in diameter. If we use the value of 4,800 corrected for possible beam misalignment, then the ratio increases to ∼0.12. Although it was not practical to perform a complete count of smaller (<0.75 μm) microcraters on the 40K sample, our SEM results suggest that the areal density of smaller microcraters is equal to, but no larger than a factor of 1.5 higher than, the number of larger microcraters. Together, these values yield a total estimated microcrater count of between 9,600 and 12,000, or ratios of counted microcraters to counted particles of 0.25–0.30. These ratios are in the same range of magnitude as those found by Fiege et al. (2019) for electrostatic acceleration of metallic Cu dust particles into silicate meteorite target materials. In evaluating their findings, Fiege et al. (2019) noted that incomplete registration of microcraters had previously been found in several other studies of dust particle impacts in silicate rock targets and other materials (Bloch et al., 1971; Hassani-Gangaraj et al., 2016; Neukum et al., 1970). Evidence from these previous studies has further suggested that at sub-critical impact speeds below approximately 1–2 km s^{-1}, particles are unable to sufficiently deform the target surface to produce well-formed microcraters and either leave shallow surface dents or deflect off the surface entirely (Bloch et al., 1971; Hassani-Gangaraj et al., 2016; Neukum et al., 1970). If our upper-limit microcrater registration ratios of 0.25–0.30 are compared to the particle speed and size distribution data in Figure 1, the ratios approximately match the ∼0.30 ratio of particles whose speeds >1 km s^{-1}, a value that is close to the sub-critical speed boundary discussed by Fiege et al. (2019) and others (Bloch et al., 1971; Hassani-Gangaraj et al., 2016; Neukum et al., 1970). The results support the interpretation that the missing microcraters in the current study result from particles that were not going fast enough to form SEM-detectable microcraters.

4.2. Effect of Slow-Particle Exclusion on Statistical Impact Speed Estimates

A primary goal of the current study was to connect the observed SEM- and TEM-scale microstructures of our experimental microcraters to the key variable of dust impactor speed. The main challenge in making this connection is statistical: our experiment varied both the speed and size of the impacting particles but not in a strongly correlated way. The practical result is that even for a narrow estimate for the likely size of the impactor that produced a given microcrater, the statistical spread in the range of likely corresponding impact speeds is still too large to get a useful constraint on what the likely impact speed was for a given microcrater. If, however, most or all of the slowest (<1 km s^{-1}) dust impactors in the 40K experiment did not form microcraters, the distribution of size and speed values within the (now smaller) particle population becomes statistically simpler, largely because the bimodal contribution from the large population of <1 km s^{-1} particles is removed from the distributions (Figures 2c and 2d). Although the correlation statistics between the particle sizes and speeds are still far from linear, and each is well-skewed relative to a normal distribution, the correlation becomes more amenable to standard statistical descriptions if the <1 km s^{-1} particles are excluded.

In Figure 11, we use a quartile box and whisker plot to depict the distribution of >1 km s^{-1} impact speeds within ascending 10th percentile intervals of corresponding particle sizes for the 40K experiment. Quartile statistics were used because they are generally considered more appropriate than means and standard deviations for describing skewed distributions that have more log-normal than normal character. Maximum shock pressures corresponding

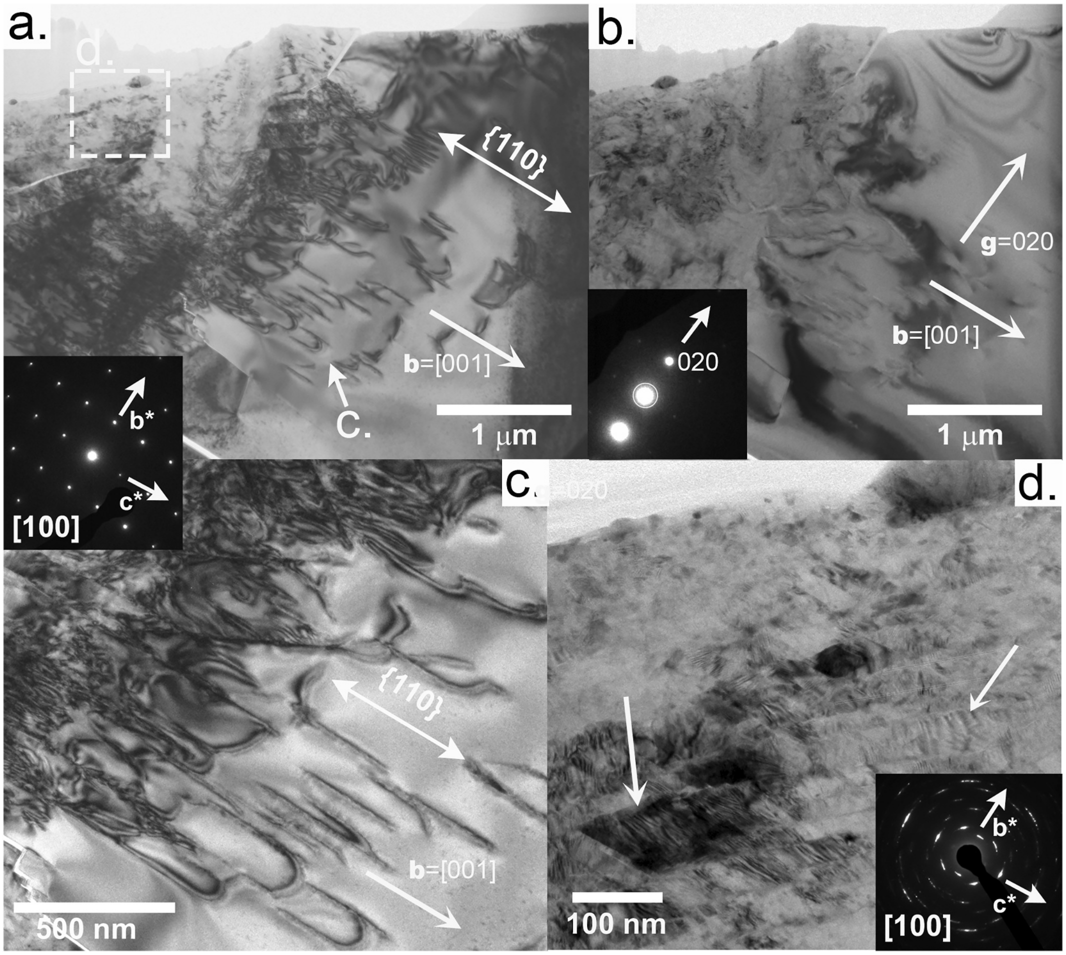

Figure 8. Conventional bright-field (BF) diffraction contrast transmission electron microscope (TEM) images of microstructures in the-to-right portion of the focused ion beam (FIB) section of microcrater #1 (see Figure 7a). (a) BF image taken in symmetrical [100] zone axis diffraction (lower left inset) orientation showing distribution of impact-induced microstructures. The double-arrow line defines the intersection between the symmetrically equivalent dislocation glide planes {110} and the plane of the FIB section. The direction of the Burgers vector b = [001] relative to the image is shown by the white arrow. (b) Same region in (a) taken under BF two-beam conditions for g = 020, with the corresponding direction of the 020 reciprocal lattice vector shown on the image (c) Enlargement of region of dislocation loops and tangles in (a) (indicated by white arrow labeled (c)) and taken under the same symmetrical [100] zone diffraction conditions as (a). (d) Conventional TEM BF image showing enlargement of inset region immediately below the microcrater floor in (a). The white arrows point to nano-scale fractures.

to the impact speed intervals as derived from our shock impedance calculations are shown on the upper horizontal axis (Figures A1 and 11; Table A2). Microcrater diameters corresponding to the dust particle size intervals on the left-hand vertical axis are shown on a secondary right-hand vertical axis scale (Figure 11). To relate particle diameter to microcrater diameter, we adjusted the 0.68 proportionality constant between dust impactor diameter and microcrater diameters in Price et al. (2010) to obtain a reasonable fit to the observed size range of microcraters in the current experiments. The adjustments evaluated the reasonableness of applying relations developed based on glass particle impacts into aluminum at a constant 6 km s^{-1} to the current case of metallic particle impacts into olivine at variable impact speeds. The results were tested against our findings that the 40 K sample contained few, if any, microcraters smaller than 0.2 μm or larger than 5.2 μm in diameter, and that the sample contained roughly sub-equal proportions of microcraters in the two intermediate size ranges of 0.75–5.2 μm and 0.2–0.75 μm. It was found that constants adjusted outside of the range between 0.5 and 0.7 predicted microcrater size distributions inconsistent with the SEM results. Separate microcrater size calibrations for the 0.5 and 0.7 proportionality constants are shown on the secondary right-hand axis of Figure 11.

10.1029/2025JE009257

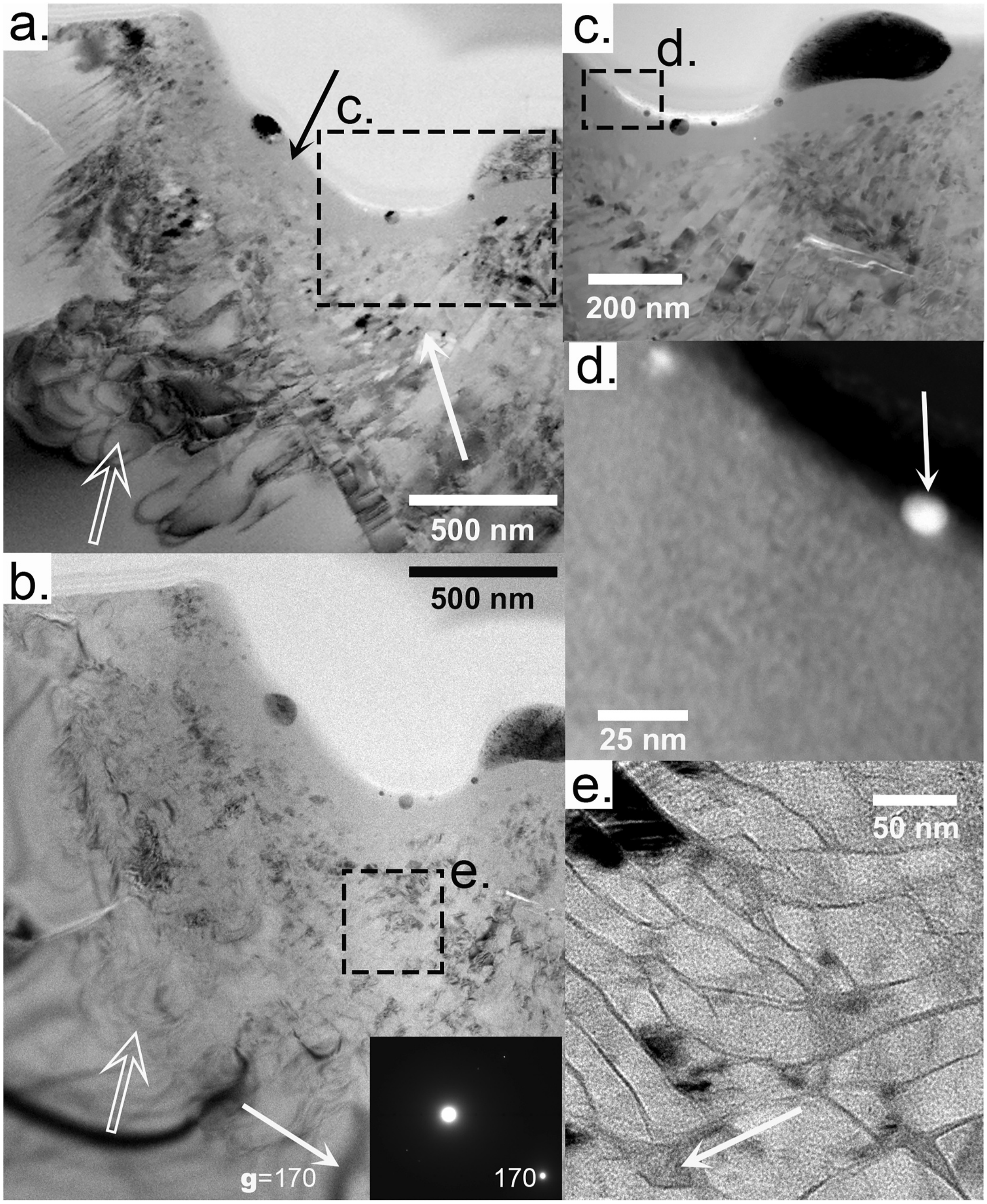

Figure 9. (a) Diffraction-contrast dark-field STEM (inverted contrast) image of the left portion of the focused ion beam section of microcrater #29 (see Figure 7b). Black arrow points to the shock melt layer lining the microcrater floor. The solid white arrow points to oriented nanofractures in the microcrater floor below the shock melt layer. Open white arrow points to dislocation pile-ups/tangles. Image taken under the symmetrical [100] zone axis diffraction condition under which only dislocations with Burger's vector $b = [001]$ are visible (open white arrow). The image in (b) shows the same area as in (a) under 2-beam conventional bright-field transmission electron microscope diffraction contrast conditions for the reflection $g = 170$. (d) high angular annular dark field image showing enlargement of microcrater shock melt glass. White arrow indicates metallic Fe spherule derived from Fe metal dust impactor. (e) Enlargement of inset in (b) showing details of oriented nanofractures whose gaps and intersection points contain amorphous material (white arrow) interpreted to be shock melt (see text).

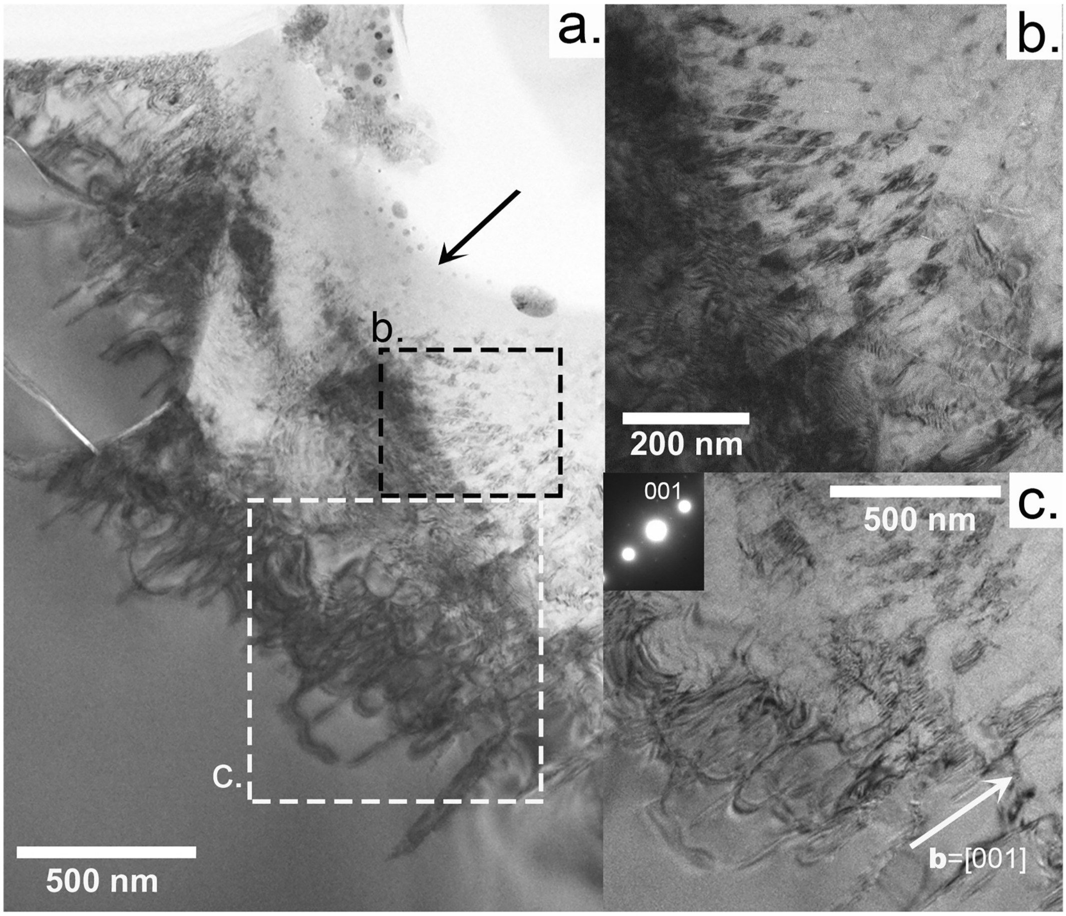

Figure 10. Conventional transmission electron microscope bright-field diffraction contrast images showing details of impact-generated microstructures in microcrater #30 (see Figure 7c). (a) Cross-section of the left portion of microcrater showing glassy lining (interpreted as shock melt) on the left wall and floor of microcrater (black arrow), oriented nanofractures in the region below the microcrater floor (dashed black rectangle, inset (b)) and dislocation pile-ups/tangles (dashed white rectangle, inset (c)). Image taken under symmetrical [100] zone axis orientation. (b) Inset showing oriented nanofractures in region below microcrater floor. (c) Inset showing abrupt boundary between dislocation pile-up/tangles (image lower left) and nanofracture network (image upper right). Image taken under two-beam conditions for the 100 reflections under which dislocations with Burgers vector b = [001] are in strong contrast.

4.3. Microcrater Shock Melting Linked to Impact Speeds and Shock Pressures

We found that shock melt generated from the olivine target material was either confirmed or likely to be present in 19 of the 31 microcraters listed in Table 1. Its presence/absence and relative amount correlated with microcrater size such that melt became more consistently present and larger in relative volume as microcrater diameters became smaller than ∼1 μm. This trend shows a possible correlation with the first significant shift to higher median impact speed (i.e., from 2.5 to 5 km s^{-1}) and corresponding higher shock pressures (from ∼40 to ∼100 GPa) that occurs as microcrater sizes decrease into the sub-micron range (Figure 11). As microcraters become still smaller, below 0.5 μm in diameter, median impact speeds extend into the 15–20 km s^{-1} range, with corresponding shock pressures more than 250 GPa for microcraters <0.32–0.45 μm in diameter (Figure 11). Microcraters within this smallest size range exhibit the largest relative volumes of shock melt compared to larger microcraters (e.g., Figures 3e–3g). To our knowledge, the SEM imaging results for these smallest microcraters are the first ever obtained for experimental microcraters whose impactor speeds could be reasonably well constrained to be in the 15–20 km s^{-1} speed range.

Although olivine shock melt was more common and larger in relative volume compared to the microcrater size in sub-micron microcraters, it was still found in half of the microcraters larger than a micrometer, including in the second largest, 5.1 μm diameter, microcrater listed in Table 1 (Figures 4a and 4c). Although these larger

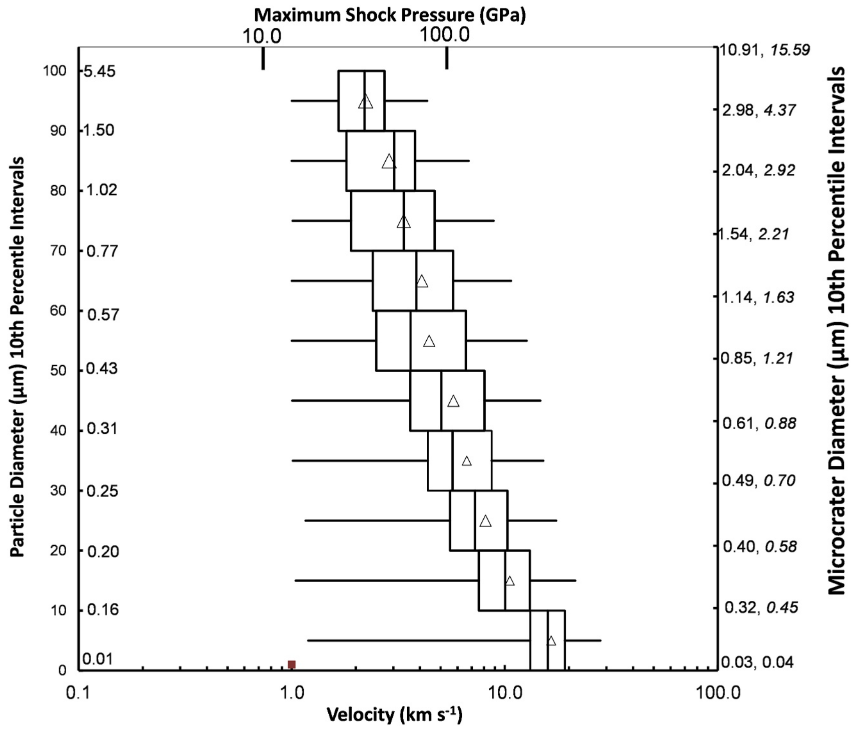

Figure 11. Box and whisker plots (see Tukey, 1977) showing a quartile-based statistical distribution of impact speeds (lower horizontal axis) and corresponding maximum shock pressures (upper horizontal axis) for 10th percentile dust particle size intervals (left vertical axis) for the 40K experiment. Data are for all particles in the experiment traveling faster than 1 km s^{-1}. Left and right sides of each box correspond to the first and third quartiles of the particle speed distribution, with the vertical line representing the median, and the open triangle representing the mean speed value. Whiskers are drawn from the box sides to the maximum and minimum speed values in the distribution. Model values for microcrater diameters corresponding to the maximum and minimum particle sizes for each 10th percentile interval are shown on the right vertical axis. Two model values are shown, one assumes a 0.5 linear proportionality between microcrater diameter and particle diameter, the other value (italics) is for a proportionality value of 0.7 (see text).

microcraters were likely made by relatively slower impactors traveling at median speeds down to ∼2 km s^{-1}, the shock impedance pressure corresponding to this lowest speed is still considerable, at ∼45 GPa (Figures A1 and 11, Table A2). This value is approximately a factor of 2 lower than the threshold value of ∼80 GPa previously reported for olivine shock melting under planar shock reverberation conditions (Bauer, 1979). The level of entropic heating achieved for equivalent maximum pressures between planar shock experiments and the single-shock conditions in the current particle impacts are different; however, with the latter being more efficient for raising both the impactor and the target above their melting points. Consequently, it is very possible that shock melting might have occurred in the current samples even for particles traveling at speeds somewhat below 2 km s^{-1}.

Finally, we point out that the calculated shock impedance pressures are maximum values localized to the point of impact. Thus, even if shock pressures were high enough to melt the target on a very local scale at the point of impact for the larger, slower particles, such small, localized amounts of melt would be less likely to be retained within the microcrater cavity. This could explain why shock melt was not found in the SEM images of several of the larger microcraters as well as in the FIB section of the largest of the three microcraters studied by TEM.

4.4. TEM-Scale Insights Into Microcrater Formation Mechanics

The same basic shock physics that produce natural macroscopic impact craters also produced the microcraters in the current study, but some special-case circumstances apply to how the single-crystal olivine target material responded to the induced shock from the impacting small particle. The most important of these is that shock and deformation occurred in an initially highly homogeneous, single-crystalline target that had the unique ability to accommodate permanent plastic deformation by the glide of dislocations. These characteristics simply do not apply to larger-scale heterogenous rock targets. Other shock and deformation processes, however, such as fracturing and shock-induced melting, are responses shared between the two scales of cratering events. Also shared, for example, would have been the excavation processes that opened the microcrater cavity due to the outward-directed excavation particle flow field generated after both the shock and rarefaction waves had passed through the target (Melosh, 1985). The ejecta removed from the cavity would have consisted of melted and/or fragmented material produced under the high-shock/high-temperature conditions generated by the shock/rarefaction wave closest to the point of impact. These same conditions would have also generated the shock melt that eventually formed the glassy cavity linings in the #29/#30 microcrater pair. The maximum shock impedence pressures we estimate for these conditions are in the range 50–100 GPa, and would have bracketed the ∼80 GPa minimum pressure for olivine shock melting under planar shock reverberations conditions (Figure A1, Table A2, Bauer, 1979). The fact that a portion of the induced shock melt was retained as a lining along the microcrater cavity may reflect the difference between outward and inward particle flows during impact, or simply the outward flows becoming too weak at that depth to eject material (Melosh, 1985). By contrast, for microcrater #1, which showed no impact melt and has lower corresponding impact speeds and shock pressures (1.5–2.5 km s^{-1} and 25–50 GPa), the amount of generated impact melt may have been too small to survive the dynamics of crater excavation.

The deformation microstructures that are present in the un-melted olivine are the product of continued radial expansion of the shock/rarefaction wave pair, whose induced stresses decay with distance from the impact point and vary with the direction of wave propagation. This latter relationship results in a greater concentration of deviatoric stress and associated elastic/plastic strain in regions closer to the crater axis, a relationship that is consistent with our observation that the nano-fractured zones in our samples are centrally concentrated below the microcrater floors. Our electron diffraction results further suggest that although the nano-fractured zone may have experienced relatively higher levels of stress and/or strain rate compared to other areas around the microcrater margins, once the nano-fracture network developed, the subsequent strain was either too small, or had too small a shear component, to substantially mis-align the resulting fragments. Overall, this is consistent with the application of near instantaneous high stress and associated strain rate that exceeded the fracture yield strength of the olivine, followed by rapid dissipation without enabling significant additional strain.

The microstructural transition that occurs between the nano-fractured zone and the dislocation-dominated zone reflects a shift from brittle-to-ductile deformation mechanisms as the stresses and/or strain rates imposed by the shock/rarefaction wave pair decay below a critical level. The spatial abruptness of the transition, occurring over distances of only 100–200 nm, may be an intrinsic reflection of the behavior of shock attenuation in the olivine sample based on its elastic/anelastic Hugoniot relations, or simply reflect fundamental aspects of the brittle-to-ductile deformation transition in olivine more generally.

The substructure of the dislocation-dominated zone itself reflects the generation and glide of dislocations in response to progressively decaying shock/rarefaction wave stresses, with only the {110}[001] slip system being active. The latter has been shown by previous studies to be the typical, but not always exclusive, system for low temperature, high strain rate deformation in olivine, including conditions occurring during shock (Carter & Ave'Lallement, 1970; Tielke et al., 2022). Our finding that dislocations tend to have longer screw segments and shorter edge segments, reflecting the tendency of loops to be elongated in the [001] Burger's vector direction, is very similar to the dislocation substructure relations found by Tielke et al. (2022) for their planar shock experiments. The substructures in either case likely reflect a basic effect of larger lattice friction on the mobility of the screw segments compared to edge segments, although more complex effects from dynamics at the shock wave front were also suggested by Tielke et al. (2022). If the deformation in the current sample had occurred at slower strain rates under non-shock conditions, continued dislocation motion would likely have removed most of the dislocation loop elongation observed in the current sample. For the current case, however, the dislocations likely did not propagate far from their sources, which may have come from fractures located at the edges of the nano-fractured zone.

4.5. Comparison to Experimental Microcraters Generated by Laser Shock

Our results offer the opportunity to compare electron microscope observations of microcraters produced by micrometer-scale projectile impacts to observations of microcraters produced by laser shock techniques, in which laser pulses are tuned to accentuate physical shock in addition to pulsed heating (Fazio et al., 2018; Langenhorst et al., 1999). Langenhorst et al. (1999) produced crater-like mm-scale shock zones in an Fo_{89} olivine single crystal from the localized impact of a thin metal flyer plate irradiated by a high-power Neodymium glass laser. They found networks of dislocations occurring on the same {110}[001] slip system as our samples, but these networks were highly localized around linear fractures that appeared to be the main source of dislocation generation. We observed some correlation between dislocations and structural discontinuities in the current samples, but we saw no evidence for fractures or other defects acting as a dominant dislocation sources.

The shock melt in our microcraters was not reported in the Langenhorst et al. (1999) sample, which was calculated to have experienced shock pressures in the 20–60 GPa range, similar to our maximum pressure estimates for our melt-bearing microcraters. This may suggest that coupling the laser to a flyer-plate in the Langenhorst et al. (1999) experiments resulted in less entropic thermal conditions for the same shock pressure, similar to what occurs when larger flyer plates are used in shock reverberaton experiments compared to single-shock projectile impacts (e.g., Tielke et al., 2022). This concept is further supported by a closer resemblance, when compared to our samples, of the laser sample microstructures to those in shock reverberation experiments (Tielke et al., 2022).

More recently, Fazio et al. (2018) described melting and shock effects in crater-like ablation pits generated in olivine by high power femtosecond laser pulses. The pits were lined with melt-derived material that had recrystallized sublayers as well as preserved glass and contained abundant nanophase metallic iron ($npFe^0$) particles. The olivine below these layers contained high densities of both microfractures and dislocations, but dislocations were absent when the shock direction was perpendicular to the [001] Burgers vector direction. The combination of densely developed microfractures closer to the sample surface with dislocation networks farther from the point of irradiation resembles the distribution of shock-induced defects (e.g., microfractures and dislocations) in our samples. This resemblance does not, however, apply to the melted portions of the laser samples, which showed clear evidence of $npFe^0$ formation during the laser irradiation, something we did not observe within the melted portions of our dust-impact samples. (As we previously noted, the larger Fe metal mounds and spherules in our samples we interpret to be the sole products of shock melting of the Fe metal dust impactor).

For their laser samples, Fazio et al. (2018) outlined a conceptual mechanism in which $npFe^0$ is produced by a complex, but essentially thermal, reduction process in which oxygen preferentially partitions out of the melt phase and into a plasma-mediated vapor plume. This results in a net chemical reduction of the less-volatile Fe in the melt. Plasma and vapor-plumes are also generated in hypervelocity projectile impacts and were undoubtedly present during the multi-stage processes of impact melting, and vaporization associated with our microcraters. It is possible, however, that the chemical dynamics of oxygen loss and associated Fe reduction within the plasma/vapor plume generated in our dust impacts were less efficient compared to those occurring in the Fazio et al. (2018) experiments. We think the most likely reason for this is simply due to the attainment of much higher temperatures in the laser irradiation. This is supported by the approximate factor of 5 larger volume of melt in the laser samples, a difference consistent with a higher net transfer of thermal energy into the sample during the laser pulse compared to what was delivered in the dust impact. The result would be higher overall thermal efficiency for driving reduction through oxygen volatilization. A future approach to evaluate this hypothesis could employ Hugoniot equation-of-state relations coupled with atomistic simulations to see if improved estimates can be placed on the stock-induced temperatures attained in microcrater impacts such as those investigated here.

Apart from the plasma/vapor plume in the laser experiments simply being hotter, the dynamics of oxygen loss in our dust impacts may also have been kinetically limited by a comparatively faster cooling rate of the relatively smaller volume of melt in contact with the cooler walls and floor of the un-melted olivine surrounding the microcrater. Therefore, the short time available to support oxygen loss by diffusion and nucleation and growth of the Fe^0 melt spherules may also have been a factor in controlling $npFe^0$ formation in the dust projectile impacts. Although we find this concept reasonable, it is somewhat in conflict with a recent finding by Chen et al. (2025), discussed further below, that $npFe^0$ is contained within the shock-melted portions of even very small natural olivine microcraters, whose size, relative amounts of shock melt, and shock features resemble our experimental samples in most respects.

4.6. Comparison to Natural Microcraters With Implications for $npFe^0$ Formation in Micrometeorite Impacts

Microcraters on the space-exposed surfaces of lunar rocks were studied extensively in the post-Apollo era primarily for the insight they provided on the flux of micrometeoroids hitting the lunar surface (Bloch et al., 1971;

Fechtig et al., 1977; Hörz et al., 1977; Morrison & Clanton, 1979; Neukum et al., 1970). The optical and more limited SEM observations that accompanied this work found most microcrater interiors contained impact melt and various styles of fracture-associated shock deformation (e.g., Fechtig et al., 1977; Morrison & Clanton, 1979; Schaal et al., 1976). SEM imaging studies have been performed more recently on microcraters occurring on a diversity of regolith grains returned from asteroids Itokawa (Harries et al., 2016; Matsumoto et al., 2018; Nakamura et al., 2012), Ryugu (Noguchi et al., 2022) and Bennu (Seifert et al., 2025), as well as on lunar rocks and regolith grains (Cymes et al., 2024; Gu et al., 2025; Noble et al., 2015). So far only a few microcraters in lunar and asteroidal samples have been cross sectioned by FIB techniques for TEM study, but the results reveal considerable diversity in the styles of microcrater shock-induced melting and deformation effects depending on the nature of the host mineral (Chen et al., 2025; Cymes et al., 2024; Gu et al., 2025; Harries et al., 2016; Noble et al., 2015).

For olivine specifically, the studies of natural microcraters that offer a comparison to our experimental results come from SEM studies of Itokawa olivine regolith samples (Matsumoto et al., 2018; Nakamura et al., 2012), and from SEM/TEM studies of microcraters in lunar olivine (Chen et al., 2025; Gu et al., 2025; Noble et al., 2015, 2016). In the Itokawa olivine grains, SEM observations reveal a diversity of microcrater morphologies, fracture microstructures and relative amounts of impact melt, with roughly half of the microcraters showing a basic resemblance to our experimental microcraters. The closest resemblance seems to occur between the smallest (0.1–0.2 μm diameter) microcraters in both the natural (Nakamura et al., 2012; Figure 2) and experimental samples (e.g., Figures 3e and 3f). Both sets have similar smooth, raised rims with chain-like arrangements of small spherules. This resemblance is consistent with the expectation that the smallest and highest impact speed (∼10–20 km s^{-1}; Figure 11) microcraters in our study would be most likely to match natural microcraters whose average impact speeds are approximately in the same range (Pokorny et al., 2019).

All the TEM studies reported to date for natural olivine microcraters are derived from four lunar microcraters (Chen et al., 2025; Gu et al., 2025; Noble et al., 2015, 2016). Gu et al. (2025) studied two sub-micron diameter olivine microcraters on lunar soil grains returned by the Chang'e-5 mission. They found complex arrangements of amorphous layers in the microcrater interiors. These included an upper layer containing a high concentration of $npFe^0$ particles and an underlying amorphous layer devoid of $npFe^0$ particles. Neither of the amorphous layers was unambiguously interpreted by the authors as a product of shock melting, with the upper layer cited as possibly being a complex product of impact melt generation from a target that already contained $npFe^0$ from previous space weathering processes.

Chen et al. (2025) studied a third sub-micron diameter olivine microcrater on another Change'e-5 soil grain and found a well-developed glassy shock melt lining 50–80 nm wide along the floor and walls of the microcrater interior. Particles of $npFe^0$ 5–10 nm in size were evenly distributed throughout the shock melt glass in a concentration of roughly 1–2 modal percent. The olivine below the shock melt layer contained a moderate density of dislocations in a shock-deformed zone approximately 200 nm wide.

A microstructurally complex, 20 μm-diameter, olivine microcrater studied by Noble et al. (2015) contained a 0.5–2.0 μm wide layer of shock melt lining its cavity and a 15–20 μm wide underlying zone of microfractures and dislocations. The shock melt glass contained $npFe^0$ particles similar in size (5–10 nm) and modal concentration to those found in the Chen et al. (2025) study. Evidence was found for limited post-impact re-growth of olivine within the melt layer, a feature resembling the recrystallized "rampart" zones in the Fazio et al. (2018) laser samples.

The TEM results for the natural olivine microcraters described by Gu et al. (2025) differ substantially from what we found for our experimental microcraters. By comparison, however, the microcraters in the Chen et al. (2025) and Noble et al. (2015) studies have distributions of shock melt and dislocation-assisted deformation, which if considered in relation to the respective microcrater sizes, broadly resemble those in our microcraters #29 and #30. The presence of $npFe^0$ particles within the shock melt portions of the natural microcraters, but not in our experimental microcraters #29 and #30, could reflect several differences between the variables controlling our results compared to those affecting the laser shock experiments as we discussed previously in §1.11. We note that the olivine microcrater studied by Chen et al. (2025), being a close match to our microcraters #29 and #30 in size and relative volume of shock melt, may have been similarly subjected to very rapid cooling. It nevertheless contains $npFe^0$ particles within its shock melt lining, an observation which, relating to our previous discussion, might tend to argue against cooling rate playing a major role in affecting $npFe^0$ formation in the shock melt during impact.

One additional variable to consider in comparing our experimental microcraters to their natural counterparts relates to the long-standing hypothesis that solar wind H implanted in lunar or asteroidal surface materials may promote $npFe^0$ formation in the products of micrometeorite impacts (e.g., Denevi et al., 2023; Housley et al., 1973; Noble et al., 2015). We performed our experiments using terrestrial San Carlos olivine samples for which the H content was previously determined to be ∼30 ppm (Bai & Kohlstedt, 1993). The net contribution of this amount of H to the formation of $npFe^0$ via the reaction:

$$\mathrm{FeO\ (in\ olivine)} + 2\mathrm{H}^+\ \mathrm{(in\ olivine)} = \mathrm{Fe}^0 + \mathrm{H_2O\ (vapor)} \quad (1)$$

would yield ∼0.02 vol. % $npFe^0$ in any associated impact melt. Such an amount, if it came only via reaction (1) or another H-associated reaction, would be difficult to detect even at the TEM scale. Although some lunar and asteroidal regolith materials have been found to have higher H contents than our experimental sample, the data vary considerably between bulk regolith with contents in the 25–75 ppm range and the space weathered rims on lunar regolith grains with contents up to 2,500 ppm H (Bustin et al., 1986; Epstein & Taylor, 1970; Xu et al., 2022). The latter amounts would be sufficient to contribute up to 3 vol. % to the net yield of $npFe^0$ from reaction (1), but the yield would be substantially lower (e.g., 0.1 to 0.2 volume %) for most of the H contents reported so far for the lunar regolith.

As it currently stands, given the uncertainties about the probable amount of H present in any given lunar or asteroidal surface material impacted by micrometeorites, as well as uncertainties about the mechanisms of the reactions involved, we are unable to ascribe the presence of $npFe^0$ in any given natural olivine microcrater, compared to our experimental ones, as being uniquely due to a difference in H content. However, by performing impact experiments on a single-crystalline material with a known H content, we consider that the current results may ultimately help to disentangle many of the open questions discussed by Denevi et al. (2023) about the role of solar wind H in $npFe^0$ formation during space weathering.

5. Conclusions

We produced estimated populations of 9,000 to 12,000 microcraters 0.2–5.2 μm in diameter on the polished surfaces of two Fo_{87} olivine crystals by exposing them to streams of electrostatically accelerated Fe metal dust particles traveling at 0.3–30 km s^{-1}. We characterized the crater morphologies and microstructures by SEM imaging and selected three microcraters for imaging and analysis by TEM. Consistent with previous electrostatic dust impact studies on mineral samples, we found evidence that impacts from particles traveling less than approximately 1 km s^{-1} did not generate SEM-visible microcraters. From statistical analysis of the size versus speed relations for the more than 1 km s^{-1} particles and the relations between microcrater diameter and impactor sizes, we were able to estimate probable impact speeds and maximum shock pressures for specific microcraters of interest. For the smallest microcraters between 0.2 and 0.5 μm in diameter, median impact speeds extend into the 15–20 km s^{-1} range, which exceeds the limits of speeds possible with conventional chemically propelled projectiles. These smallest microcraters contain abundant shock melted olivine generated at estimated maximum shock pressures more than 250 GPa. Shock melt was also found to be lining the cavities of 2 of the 3 microcraters studied by TEM, but no metallic Fe nanoparticles (i.e., $npFe^0$) were present in this melt. Shock deformation of the un-melted olivine in the TEM samples occurred by a combination of dense microfracturing immediately below the microcrater floor, and plastic deformation by dislocation glide beyond the microfractured region. Dislocation glide occurred exclusively on the {110}[001] slip system previously known to be characteristic for olivine deformation at low temperatures and high strain rates. Restriction to this single slip system combined with lower mobility of the screw component of dislocations indicates that the amount and distribution of shock-induced ductile strain for small scale impacts in olivine grains will be strongly dependent on the crystallographic direction of a given impact. The two melting-bearing microcraters studied by TEM, neither of which contain $npFe^0$, are estimated to have formed at impact speeds of 3.0–3.5 km s^{-1} and maximum shock pressures of 50–60 GPa.

Appendix A: Maximum Shock Pressures for Dust Particle Impact Speeds Derived From Shock Impedance Calculations

Table A1
Input Parameters for Shock Impedance Calculations

Material	a (km s^{-1})[a]	b[b]	Density (g cm^{-3})	Min U_P (km s^{-1})	Max U_P (km s^{-1})
Olivine (elastic)[c]	8.84	−0.099	3.264	0.272	1.43
Olivine (low pressure)[c]	5.6	1.3	3.264	1.43	2.19
Olivine (mixed region)[c]	8.1	0.15	3.264	2.19	2.8
Olivine (high pressure)[c]	6	0.88	3.264	2.8	4.81
Iron[d]	3.574	1.92	7.86		

[a]Bulk sound speed. [b]Coefficient. [c]Values from Ahrens and Johnson (1994) for their different shock regimes (e.g., elastic; low pressure). [d]Values from Marsh (1980).

Table A2
Maximum Shock Pressures (P) Generated in Olivine Target From Fe Metal Dust Impactor

Olivine (elastic)			Olivine (low pressure)			Olivine (mixed region)			Olivine (high pressure)		
V (km s^{-1})[a]	U_P	P (GPa)	V	U_P	P	V	U_P	P	V	U_P (particle)	P
0.50	0.26	7.54	2.30	1.44	35.19	3.50	2.22	60.98	4.40	2.86	79.36
0.60	0.32	9.13	2.40	1.51	37.16	3.60	2.29	62.99	4.50	2.92	81.80
0.70	0.37	10.75	2.50	1.57	39.16	3.70	2.36	65.01	4.60	2.99	84.27
0.80	0.43	12.39	2.60	1.63	41.20	3.80	2.43	67.04	4.70	3.06	86.77
0.90	0.49	14.06	2.70	1.70	43.28	3.90	2.50	69.08	4.80	3.13	89.30
1.00	0.55	15.74	2.80	1.76	45.39	4.00	2.57	71.14	4.90	3.19	91.85
1.10	0.61	17.44	2.90	1.83	47.54	4.10	2.64	73.20	5.00	3.26	94.43
1.20	0.67	19.16	3.00	1.89	49.73	4.20	2.71	75.28	5.10	3.33	97.04
1.30	0.73	20.90	3.10	1.95	51.95	4.30	2.78	77.36	5.20	3.40	99.68
1.40	0.79	22.65	3.20	2.02	54.21				5.30	3.47	102.35
1.50	0.85	24.42	3.30	2.08	56.50				5.40	3.53	105.05
1.60	0.92	26.20	3.40	2.15	58.83				5.50	3.60	107.77
1.70	0.98	28.00							5.60	3.67	110.52
1.80	1.05	29.80							5.70	3.74	113.30
1.90	1.11	31.62							5.80	3.81	116.10
2.00	1.17	33.45							5.90	3.87	118.94
2.10	1.24	35.29							6.00	3.94	121.80
2.20	1.31	37.15							6.10	4.01	124.69
2.30	1.37	39.01							6.50	4.28	136.53
2.40	1.44	40.88							7.00	4.62	151.96
									8.00	5.31	184.91
									9.00	6.00	220.65
									10.00	6.68	259.18

[a]Dust particle impact speed.

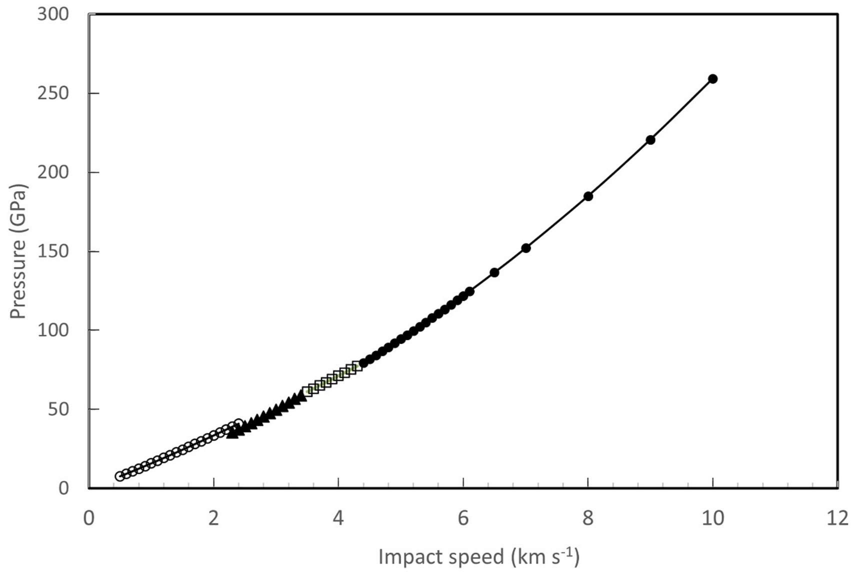

Figure A1. Plot of Table A2 maximum shock pressures versus impact speed values.

Conflict of Interest

The authors declare no conflicts of interest relevant to this study.

Data Availability Statement

The transmission and scanning electron microscope images and raw IMPACT facility dust accelerator data used in the preparation of the figures in this paper are at Zenodo: https://doi.org/10.5281/zenodo.16376320 (Christoffersen, 2025-2026). The MATLAB version R2023a code used to create Figure 1 using licensed MATLAB software (https://www.mathworks.com/products/matlab.html) is also available in MATLAB and.txt formats also at ZENODO: https://doi.org/10.5281/zenodo.16376320 (Christoffersen, 2025-2026).

Acknowledgments

This work was supported by NASA Solar System Workings Grant NNX16AH40G to Mark J. Loeffler. The IMPACT Laboratory Dust Accelerator Facility at the University of Colorado was supported under NASA SSERVI Grant 80NSSC19M0217. This work was supported in part by the Johnson Space Center Coordinated Analysis Work Package funded by the NASA Internal Scientist Funding Model. Helpful discussions and comments on earlier versions of the paper were provided by F. Hörz and B. Cymes.Additional review comments by D. Harries and an anonymous reviewer greatly improved the paper. D. Thompson provided helpful assistance with Figure 1 data plotting and graphics.

References

Ahrens, T. J., & Johnson, M. L. (1994). Shock wave data for minerals. *NASA CR*, 199490.

Altobelli, N., Fiege, K., Carry, B., Soja, R., Guglielmino, M., Trieloff, M., et al. (2019). Space weathering induced via microparticle impacts: 1. Modeling of impact velocities and flux of micrometeoroids from cometary, asteroidal, and interstellar origin in the main asteroid belt and the near-earth environment. *Journal of Geophysical Research (Planets)*, *124*(4), 1044–1083. https://doi.org/10.1029/2018JE005563

Bai, Q., & Kohlstedt, D. L. (1993). Effects of chemical environment on the solubility and incorporation mechanism for hydrogen in olivine. *Physics and Chemistry of Minerals*, *19*(7), 460–461. https://doi.org/10.1007/BF00203186

Barber, D. J., Wenk, H. R., Hirth, G., & Kohlstedt, D. L. (2010). Dislocations in minerals. In J. P. Hirth & L. Kubin (Eds.), *Dislocations in solids* (pp. 171–232). Elsevier B. V.

Bauer, J. F. (1979). Experimental shock metamorphism of mono- and polycrystalline olivine: A comparative study. *Proceedings of the 10th Lunar and Planetary Science Conference*, 2573–2596. https://articles.adsabs.harvard.edu/full/1979LPSC…10.2573B

Bloch, M. R., Fechtig, H., Gentner, W., Neukum, G., & Schneider, E. (1971). Meteorite impact craters, crater simulations, and the meteoroid flux in the early solar system. In *Proceedings of the 2nd lunar science conference* (Vol. 3, pp. 2639–2652). Retrieved from https://articles.adsabs.harvard.edu/full/1971LPSC....2.2639B

Bustin, R., Carr, R. H., Gibson, E. K., & Sommer, M. A. (1986). The hydrogen content of lunar soils. *Lunar and Planetary Science Conference*, 95–96.

Carter, C. B., & Ave'Lallement, H. G. (1970). High temperature flow of dunite and peridotite. *GSA Bulletin*, *81*(8), 2181–2202. https://doi.org/10.1130/0016-7606(1970)81[2181:HTFODA]2.0.CO;2

Chen, Y., Cao, Z., Li, C., Li, Y., Han, Z., Wang, X., et al. (2025). Characteristics of weak space weathering in Chang'e-5 lunar soil: Evidence from microcra-ters formed by low-speed impacts. *Journal of Geophysical Research: Planets*, *130*(10), e2025JE009293. https://doi.org/10.1029/2025JE009293

Christoffersen, R. (2025-2026). Experimental hypervelocity dust impacts in olivine – Multiscale insights into microcrater shock and melting effects from coordinated SEM/TEM observations. https://doi.org/10.5281/zenodo.16376320

Cliff, G., & Lorimer, G. W. (1975). The quantitative analysis of thin specimens. *Journal of Microscopy*, *103*(2), 203–207. https://doi.org/10.1111/j.1365-2818.1975.tb03895.x

Cymes, B. A., Noble, S. K., Christoffersen, R., Erickson, T., & Keller, L. P. (2024). Multi-scale analysis of an ilmenite microcrater in lunar sample 71055. *55th Lunar and Planetary Science Conference*, *1095*. https://www.hou.usra.edu/meetings/lpsc2024/pdf/1095.pdf

Denevi, B. W., Noble, S. K., Christoffersen, R., Thompson, M. S., Glotch, T. D., Blewett, D. T., et al. (2023). Space weathering at the Moon. In C. R. Neal, L. R. Gaddis, B. L. Jolliff, S. J. Lawrence, S. J. Mackwell, C. K. Shearer, et al. (Eds.), *New views of the moon 2* (pp. 611–650). Mineralogical Society of America. https://doi.org/10.1515/9781501519895-017

Epstein, S., & Taylor, H. P., Jr. (1970). The concentration and isotopic composition of hydrogen, carbon and silicon in Apollo 11 lunar rocks and minerals. *Geochimica et Cosmochimica Acta*, 1085.

Fazio, A., Harries, D., Matthäus, G., Mutschke, H., Nolte, S., & Langenhorst, F. (2018). Femtosecond laser irradiation of olivine single crystals: Experimental simulation of space weathering. *Icarus*, *299*, 240–252. https://doi.org/10.1016/j.icarus.2017.07.025

Fechtig, H., Gentner, W., Hartung, J. B., Nagel, K., Neukum, G., Schneider, E., et al. (1977). Microcraters on lunar samples. In J. H. Pomeroy & N. J. Hubbard (Eds.), *The Soviet-American conference on the cosmochemistry of the moon and planets, part 2* (pp. 585–603). National Aeronautics and Space Administration.

Fiege, K., Guglielmino, M., Altobelli, N., Trieloff, M., Srama, R., & Orlando, T. M. (2019). Space weathering induced via microparticle impacts: 2. Dust impact simulation and meteorite target analysis. *Journal of Geophysical Research: Planets*, *124*(4), 1084–1099. https://doi.org/10.1029/2018JE005564

Fournelle, J. H. (2011). An investigation of "San Carlos Olivine": Comparing USNM-distributed material with commercially available material. *Microscopy and Microanalysis*, *17*(Suppl. 2), 842–843. https://doi.org/10.1017/S1431927611005083

Grun, E., Horányi, M., & Sternovsky, Z. (2011). The lunar dust environment. *Planetary and Space Science*, *59*(14), 1672–1680. https://doi.org/10.1016/j.pss.2011.04.005

Gu, L., Lin, Y., Chen, Y., Xu, Y., Tang, X., & Li, J. (2025). Submicron-scale craters on Chang'e-5 lunar soils: Records of complex space weathering processes. *Geochimica et Cosmochimica Acta*, *398*, 139–151. https://doi.org/10.1016/j.gca.2025.04.004

Hapke, B. (2001). Space weathering from mercury to the asteroid belt. *Journal of Geophysical Research: Planets*, *106*(E5), 10039–10073. https://doi.org/10.1029/2000JE001338

Harries, D., Yakame, S., Karouji, Y., Uesugi, M., & Langenhorst, F. (2016). Secondary submicrometer impact cratering on the surface of asteroid 25143 itokawa. *Earth and Planetary Science Letters*, *450*, 337–345. https://doi.org/10.1016/j.epsl.2016.06.033

Hassani-Gangaraj, M., Veysset, D., Nelson, K. A., & Schuh, C. A. (2016). Supersonic impact of metallic micro-particles. *xrXiv preprint at arXiv 1612.8081. zr*. https://doi.org/10.48550/arXiv.1612.08081

Head, A. K., Humble, P., Clarebrough, L. M., Morton, A. J., & Forwood, C. T. (1973). Computed electron micrographs and defect identification. In S. Amelinckx, R. Gevers, & J. Hihoul (Eds.), *Defects in crystalline solids*. North-Holland Publishing Company.

Hillier, J. K., Sternovsky, Z., Armes, S. P., Fielding, L. A., Postberg, F., Bugiel, S., et al. (2012). Impact ionisation mass spectra of polypyrrole-coated pyrrhotite microparticles. *European Planetary Science Congress*, *8*, EPSC2013-567.

Hirsch, P., Howie, A., Nicholson, R. B., Pashley, D. W., & Whelan, M. J. (1977). *Electron microscopy of thin crystals*. Robert E. Krieger Publishing.

Hörz, F., Morrison, D. A., Gault, D. E., Oberbeck, V. R., Quaide, W. L., Vedder, J. F., et al. (1977). The micrometeoroid complex and evolution of the lunar regolith. In J. H. Pomeroy & N. J. Hubbard (Eds.), *The soviet-american conference on the cosmochemistry of the moon and planets, part 2* (pp. 605–635). National Aeronautics and Space Administration.

Housley, R., Cirlin, E. H., & Grant, R. W. (1973). Origin and characteristics of excess Fe metal in lunar glass welded aggregates. *Proceedings of the 4th Lunar Science Conference*, *3*, 2737–2750.

Langenhorst, F., Boustie, M., Migault, A., & Romain, J. P. (1999). Laser shock experiments with nanoseconds pulses: A new tool for the reproduction of shock defects in olivine. *Earth and Planetary Science Letters*, *173*(3), 333–342. https://doi.org/10.1016/S0012-821X(99)00224-1

Li, Y. W., Bugiel, S., Trieloff, M., Hillier, J. K., Postberg, F., Price, M. C., et al. (2014). Morphology of craters generated by hypervelocity impacts of micron-sized polypyrrole-coated olivine particles. *Meteoritics & Planetary Sciences*, *49*(8), 1375–1387. https://doi.org/10.1111/maps.12338

Marsh, S. P. (1980). *LASL shock Hugoniot data* (Vol. 5). University of California Press.

Matsumoto, T., Hasegawa, S., Nakao, S., Sakai, M., & Yurimoto, H. (2018). Population characteristics of submicrometer-sized craters on regolith particles from asteroid Itokawa. *Icarus*, *303*, 22–23. https://doi.org/10.1016/j.icarus.2017.12.017

Melosh, H. J. (1985). Impact cratering mechanics: Relationship between the shock wave and excavation flow. *Icarus*, *62*(2), 339–343. https://doi.org/10.1016/0019-1035(85)90129-0

Mocker, A. A., Bugiel, S., Auer, S., Baust, G. G., Collette, A. A., Drake, K. J., et al. (2011). A 2 mv van de graaff accelerator as a tool for planetary and impact physics research. *Review of Scientific Instruments*, *82*(9), 5111. https://doi.org/10.1063/1.3637461

Morrison, D. A., & Clanton, U. S. (1979). Properties of microcraters and cosmic dust of less than 1000 å dimensions. *Proceedings of the 10th Lunar and Planetary Science Conference*, 1649–1663. https://ui.adsabs.harvard.edu/abs/1979LPSC…10.1649M/abstract

Nakamura, E., Makishima, A., Moriguti, T., Kobayashi, K., Tanaka, R., Kunihiro, T., et al. (2012). Space environment of an asteroid preserved on micrograins returned by the hayabusa spacecraft. *Proceedings of the National Academy of Sciences*, *109*(11), E624–E629. https://doi.org/10.1073/pnas.1116236109

Nakamura, T., Noguchi, T., Tanaka, M., Zolensky, M. E., Kimura, M., Tsuchiyama, A., et al. (2011). Itokawa dust particles: A direct link between S-type asteroids and ordinary chondrites. *Science*, *333*(6046), 1113–1116. https://doi.org/10.1126/science.1207758

Neukum, G., Mehl, A., Fechtig, H., & Zähringer, J. (1970). Impact phenomena of micrometeorites on lunar surface material. *Earth and Planetary Science Letters*, *8*(1), 31–35. https://doi.org/10.1016/0012-821X(70)90095-6

Noble, S. K., Keller, L. P., Christoffersen, R., & Rahman, Z. (2015). The microstructure of a micrometeorite impact into lunar olivine. In *Space weathering of airless bodies: An integration of remote sensing data, laboratory experiments and sample analysis workshop, 2034*. The Lunar and Planetary Institute. Retrieved from https://ui.adsabs.harvard.edu/abs/2015LPICo1878.2034N/abstract

Noble, S. K., Keller, L. P., Christoffersen, R., & Rahman, Z. (2016). The microstructure of lunar micrometeorite impact craters. *The 47th Lunar and Planetary Science Conference*, *1465*. https://www.hou.usra.edu/meetings/lpsc2016/pdf/1465.pdf

Noguchi, T., Matsumoto, T., Miyake, A., Igami, Y., Haruta, M., Saito, H., et al. (2022). A dehydrated space-weathered skin cloaking the hydrated interior of ryugu. *Nature Astronomy*, *7*, 170–181. https://doi.org/10.1038/s41550-022-01841-6

Pokorný, P., Janches, D., Sarantos, M., Szalay, J. R., Horányi, M., Nesvorný, D., & Kuchner, M. J. (2019). Meteoroids at the Moon: Orbital properties, surface vaporization, and impact ejecta production. *Journal of Geophysical Research : Planets*, *124*(3), 752–778. https://doi.org/10.1029/2018je005912

Price, M. C., Kearsley, A. T., Burchell, M. J., Hörz, F., Borg, J., Bridges, J. C., et al. (2010). Comet 81P/Wild 2: The size distribution of finer (sub-10 μm) dust collected by the Stardust spacecraft. *Meteoritics & Planetary Sciences*, *45*(9), 1409–1428. https://doi.org/10.1111/j.1945-5100.2010.01104.x

Sasaki, S., Nakamura, K., Hamabe, Y., Kurahashi, E., & Hiroi, T. (2001). Production of iron nanoparticles by laser irradiation in a simulation of lunar-like space weathering. *Nature*, *410*(6828), 555–557. https://doi.org/10.1038/35069013

Schaal, R. B., Hoerz, F., & Gibbons, R. V. (1976). Shock metamorphic effects in lunar microcraters. In *Proceedings of the 7th lunar and planetary science conference* (pp. 1039–1054). Retrieved from https://articles.adsabs.harvard.edu/full/1976LPSC....7.1039S

Scott, D. W. (1979). On optimal and data-based histograms. *Biometrika*, *66*(3), 605–610. https://doi.org/10.1093/biomet/66.3.605

Seifert, L. B., Keller, L. P., Thompson, M. S., Rahman, Z., Connolly, H. C., Jr., & Lauretta, D. S. (2025). Coordinated analysis of microcraters in Bennu samples. *56th Lunar and Planetary Science Conference*, *1528*. https://www.hou.usra.edu/meetings/lpsc2025/pdf/1528.pdf

Shu, A., Collette, A. A., Drake, K. J., Grün, E., Horányi, M., Kempf, S., et al. (2012). 3 mv hypervelocity dust accelerator at the colorado center for lunar dust and atmospheric studies. *Review of Scientific Instruments*, *83*(7), 075108. https://doi.org/10.1063/1.4732820

Taylor, L. A., Pieters, C., Keller, L. P., Morris, R. V., & McKay, D. S. (2001). Lunar mare soils: Space weathering and the major effects of surface-correlated nanophase Fe. *Journal of Geophysical Research*, *106*(E11), 27985–27999. https://doi.org/10.1029/2000JE001402

Tielke, J. A., Peslier, A. H., Christoffersen, R., Erickson, T. M., Cline, C. J., Jakubek, R. S., et al. (2022). Dislocation generation in experimentally shocked olivine crystals. *Journal of Geophysical Research: Planets*, *127*(6), e2021JE007042. https://doi.org/10.1029/2021JE007042

Tukey, J. S. (1977). *Exploratory data analysis*. Addison-Wesley.

Williams, D. B., & Carter, C. B. (1996). Imaging in the TEM. In *Transmission electron microscopy*. Springer. https://doi.org/10.1007/978-1-4757-2519-3_22

Xu, Y., Tian, H.-C., Zhang, C., Chaussidon, M., Lin, Y., Hao, J., et al. (2022). High abundance of solar wind-derived water in lunar soils from the middle latitude. *Proceedings of the National Academy of Sciences*, *119*(51), e2214395119. https://doi.org/10.1073/pnas.2214395119